The Solution Structure, Binding Properties, and Dynamics of the Bacterial Siderophore-binding Protein FepB

Chu, Byron C. H.; Otten, Renee; Krewulak, Karla D.; Mulder, Frans A.A.; Vogel, Hans J.

Published in:
The Journal of Biological Chemistry

DOI:
10.1074/jbc.M114.564021

Publication date:
2014

THE JOURNAL OF BIOLOGICAL CHEMISTRY VOL. 289, NO. 42, pp. 29219–29234, October 17, 2014

The Solution Structure, Binding Properties, and Dynamics of the Bacterial Siderophore-binding Protein FepB*

Received for publication, March 8, 2014, and in revised form, August 27, 2014 Published, JBC Papers in Press, August 29, 2014, DOI 10.1074/jbc.M114.564021

Byron C. H. Chu[‡], **Renee Otten**[§1], **Karla D. Krewulak**[‡], **Frans A. A. Mulder**[§¶], **and Hans J. Vogel**[‡2]

From the [‡]*Biochemistry Research Group, Department of Biological Sciences, University of Calgary, Alberta T2N 1N4, Canada, the* [§]*Groningen Biomolecular Sciences and Biotechnology Institute, University of Groningen, 9747 AG Groningen, The Netherlands, and the* [¶]*Interdisciplinary Nanoscience Center (iNANO) and Department of Chemistry, University of Aarhus, 8000 Aarhus C, Denmark*

Background: FepB is a periplasmic binding protein that transports the catecholate siderophore enterobactin.
Results: The solution NMR structures of apo- and holo-FepB were solved revealing a unique siderophore binding mechanism.
Conclusion: Enterobactin binding involves the ordering of dynamic loop residues.
Significance: The binding of enterobactin by FepB does not proceed by the typical Venus flytrap scheme.

The periplasmic binding protein (PBP) FepB plays a key role in transporting the catecholate siderophore ferric enterobactin from the outer to the inner membrane in Gram-negative bacteria. The solution structures of the 34-kDa apo- and holo-FepB from *Escherichia coli*, solved by NMR, represent the first solution structures determined for the type III class of PBPs. Unlike type I and II PBPs, which undergo large "Venus flytrap" conformational changes upon ligand binding, both forms of FepB maintain similar overall folds; however, binding of the ligand is accompanied by significant loop movements. Reverse methyl cross-saturation experiments corroborated chemical shift perturbation results and uniquely defined the binding pocket for gallium enterobactin (GaEnt). NMR relaxation experiments indicated that a flexible loop (residues 225–250) adopted a more rigid and extended conformation upon ligand binding, which positioned residues for optimal interactions with the ligand and the cytoplasmic membrane ABC transporter (FepCD), respectively. In conclusion, this work highlights the pivotal role that structural dynamics plays in ligand binding and transporter interactions in type III PBPs.

Bacteria secrete ferric-iron specific chelators called siderophores to form tight complexes with iron. The three main categories of siderophores are typed based on the functional groups that coordinate the iron atom: catecholate, hydroxamate, and carboxylates (1). The most ubiquitous siderophore found among enteric bacteria, including *Escherichia coli*, is enterobactin (Ent)[3] (or enterochelin), which has an extremely high affinity for ferric iron (Fe^{3+}, $\sim 10^{-49}$ M) (2). Recent awareness of the "battle for iron" between host and pathogenic organisms has brought increased attention to the relationship between Ent (and its derivatives) and host immune molecules (*e.g.* siderocalins) (3–6). In *E. coli*, EntE, EntB, and EntF produce Ent via non-ribosomal peptide synthesis from 2,3-dihydroxybenzoic acid and serine (7). Once secreted, Ent is able to scavenge Fe^{3+} to form $[Fe^{III}(Ent)]^{3-}$, which can be taken up via the ferric enterobactin (Fep) transport system. This pathway comprises the proteins FepA, FepB, and FepCD, which are a TonB-dependent outer membrane transporter, a periplasmic binding protein (PBP), and an inner membrane ABC-dependent transporter, respectively (8). The crystal structure of FepA (9) does not conclusively reveal a $[Fe^{III}(Ent)]^{3-}$ (ferric enterobactin (FeEnt)) binding site; however, subsequent mutagenesis studies have identified important hydrophobic and electrostatic contributions to FeEnt binding at surface protruding loop residues (10, 11).

In this study, we present the solution structure, ligand binding, and dynamic properties of the FepB protein as determined by nuclear magnetic resonance (NMR) spectroscopy. FepB is a predicted type III PBP that is able to bind FeEnt, after it has been transported into the periplasm through FepA, and deliver it to its cytoplasmic membrane ABC transporter, FepCD. Periplasmic or substrate-binding proteins can be categorized broadly into three structural classes based on the number of connecting elements between the two protein lobes (12). Type III PBPs are characterized by a single α-helical linker connecting the N- and C-terminal lobes, whereas types I and II have three and two interlobal β-strands or extended elements, respectively. Apo forms of type I and II PBPs have been shown to adopt an "open" conformation, where the lobes are far apart, whereas ligand-

* This work was supported by an operating grant from the Canadian Institutes of Health Research (Novel Alternatives to Antibiotics program).
The atomic coordinates and structure factors (codes 2M6K and 2M6L) have been deposited in the Protein Data Bank (http://wwpdb.org/).
NMR backbone chemical shift assignments for apo- and holo-FepB have been deposited in the Biological Magnetic Resonance Data Bank (BMRB) under accession code 19143.
[1] Current address: Dept. of Biochemistry, Brandeis University, Waltham, MA 02454.
[2] Recipient of a Scientist Award from Alberta Innovates Health Solutions. To whom correspondence should be addressed: Biochemistry Research Group, Dept. of Biological Sciences, University of Calgary, 2500 University Dr. N.W., Calgary, Alberta T2N 1N4, Canada. Tel.: 403-220-6006; Fax 403-289-9311; E-mail: vogel@ucalgary.ca.

[3] The abbreviations used are: Ent, enterobactin; GaEnt, gallium enterobactin; FeEnt, ferric enterobactin; FeVib, ferric vibriobactin; CSP, chemical shift perturbation; HSQC, heteronuclear single quantum coherence; PBP, periplasmic binding protein; PDB, Protein Data Bank; RDC, residual dipolar coupling; r.m.s.d., root mean square deviation; TROSY, transverse relaxation-optimized spectroscopy; SASA, solvent-accessible surface area; ncSPC, neighbor-corrected structural propensity calculator.

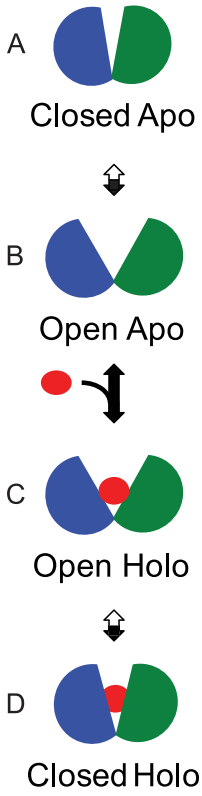

FIGURE 1. **The Venus flytrap model of ligand binding by periplasmic binding proteins.** There is a kinetic equilibrium between the closed apo (*A*) and open apo (*B*) states. In the absence of ligand, the open apo conformation is heavily favored, but upon ligand binding the protein briefly adopts an open holo state (*C*) before shifting toward the favored closed holo state (*D*). The two lobes of the protein are represented in *green* and *blue* with the ligand in *red*.

bound (holo) forms undergo a structural change to a more "closed" conformation (*i.e.* the lobes are close together). This is commonly referred to as the Venus flytrap model, wherein the apo-open PBP encounters a ligand in its binding cleft, an interaction that triggers a conformational change leading to both lobes of the protein clamping down on the ligand and stabilizing the holo-closed state (13, 14) (Fig. 1). For example, the apo-to-holo transition for the type I PBP maltodextrin-binding protein involves a (~35°) rigid body hinge-closing motion that reorients the lobes of the protein without significantly affecting their overall fold (15, 16). Similarly, for type II PBPs, large hinge-bending motions on the order of ~40° have been reported for the glutamine-binding protein (17). For type III PBPs that bind siderophores or related ligands, it is currently unresolved as to whether these proteins are able to undergo similar large scale conformational changes. The crystal structures for some type III PBP systems (*e.g.* FhuD (18) and ShuT (19)) show little to no lobe-closing motions upon ligand binding, whereas others (*e.g.* BtuF (20), FeuA (21), and HmuT (22)) show modest (~10–20°) C-terminal lobe/domain-tilting movements. Thus it is unclear whether a consensus ligand-binding mode for these proteins exists.

To date, type III PBP structures have been solved exclusively by x-ray crystallography. It is conceivable that crystal-packing forces can affect the conformation and ligand binding properties of these proteins, because molecular dynamics simulations of FhuD (18), BtuF (23), and ShuT/PhuT (24) show considerably more opening-closing transitions than the crystal structures alone. Characterization of the type III PBPs by solution methods such as NMR spectroscopy would provide new insights and perspective on the PBP field. In support of this idea, solution NMR spin relaxation (25) and residual dipolar coupling experiments (26) of maltodextrin-binding protein have revealed significant differences in degree of domain closure upon ligand binding when compared with crystal structure studies of the same protein (27). Consequently, NMR studies of FepB are expected to reveal important details with regard to the protein dynamics of type III PBPs associated with siderophore binding and release.

In this work, we report the NMR-derived solution structures of the 34-kDa apo-and holo-FepB. For our NMR studies, because of the relatively large size of the protein we utilized perdeuteration (28), transverse relaxation-optimized spectroscopy (TROSY) (29), comprehensive methyl labeling (30), and sparse NOE data from Ile(δ1), Leu, and Val methyl-labeled constructs (31, 32). The mapping of backbone and methyl chemical shift perturbations between the apo and holo states indicated the identity and regions involved in ligand binding. Hydrophobic residues directly involved in ligand binding were identified by reverse methyl cross-saturation experiments, whereas NMR spin relaxation data suggested a mechanism by which FepB would be able to bind/release its ligand that differs from the Venus flytrap model. Taken together, our results point to a distinct mode of ligand binding and release for type III PBPs.

EXPERIMENTAL PROCEDURES

Protein Expression and Purification—Mature *fepB* (33) without its signal sequence was cloned into pET-19b (Novagen) and expressed with an N-terminal His_{10} tag as described previously (30). For unlabeled FepB, cells were grown in Luria-Bertani medium, and for isotope-labeled FepB, cells were grown in M9 minimal medium in 99.9% D_2O (Sigma-Aldrich) with 1 g/liter $^{15}NH_4Cl$ (Cambridge Isotope Laboratories Inc. (CIL Inc.)) and with or without 3 g/liter [^{1}H,^{13}C]D-glucose (CIL Inc.). U-^{2}H,^{15}N;Ileδ1-{$^{13}CH_3$};Leu,Val-{$^{13}CH_3$/$^{12}CD_3$}-labeled FepB (ILV-FepB) was prepared using $^{15}NH_4Cl$ (CIL Inc.), [^{2}H,^{12}C]D-glucose (CIL Inc.), and the methyl-labeling precursors 2-keto-3-methyl-d_3-3-d_1-4-^{13}C-butyrate and 2-keto-3-d_2-4-^{13}C,d_1-butyrate (CIL Inc.) (34). Unlabeled FepB was expressed in *E. coli* BL21(DE3). U-[^{15}N]^{1}H/^{2}H-, U-[^{13}C,^{15}N]^{1}H/^{2}H-, and ILV-FepB samples were expressed in an *E. coli* BL21(DE3) Δ*entA* strain, as the longer growth times necessitated suppression of native enterobactin synthesis, which was achieved by the deletion of the *entA* gene (35). ILV-FepB samples also required an additional gel filtration chromatography purification step to remove undesired protein contaminants that arose from the longer growth period required to reach induction. For gel filtration chromatography, samples in 50 mM sodium phosphate (pH 6.4), 300 mM NaCl were applied to a HiPrep 16/60 S100 column using an ÄKTA™ FPLC (GE Healthcare Life Sciences). Holo-FepB samples were prepared by adding either $[Ga^{III}(Ent)]^{3-}$ (gallium enterobactin (GaEnt)) or FeEnt to apo-FepB as described previously (30). Iron-free enterobactin was

obtained from Biophore Research Products (University of Tübingen, Germany).

Fluorescence Spectroscopy—Fluorescence titration experiments of FepB with FeEnt or GaEnt were performed on a Varian Cary Eclipse fluorescence spectrophotometer with excitation and emission slit widths set to 5 nm. Emission spectra were recorded with an excitation wavelength of 280 nm. A protein concentration of 10 μM in 50 mM sodium phosphate (pH 6.4) was used, and all experiments were performed at 25 °C. Quenching of fluorescence intensity upon the addition of ligand was plotted as a function of ligand concentration using CaLigator (36) and a single binding site model.

Proteinase Protection Assay—Twenty μg of either apo- or holo-FepB (Fe/GaEnt) sample was incubated in the presence of proteinase K in 5 mM Tris (pH 8.0) at 55 °C as described previously (37). After 10 or 40 min of incubation, tricholoroacetic acid was added to a final concentration of 10 % (v/v), and each tube was placed at 4 °C for 5 min to quench the reaction. Precipitated protein was then resuspended in loading buffer and analyzed on 12% SDS-PAGE.

NMR Spectroscopy—NMR experiments were performed at 25 °C on Varian Unity Inova (600 and 800 MHz) or Bruker Avance (600 and 700 MHz) four-channel spectrometers equipped with a triple resonance room temperature (Varian 600/800 and Bruker 600 MHz) or a cryogenically cooled (700 MHz) probe head with pulsed field gradient capabilities. FepB samples contained ~1 mM protein in 50 mM sodium phosphate (pH 6.4), 0.5 mM 2,2,-dimethyl-2-silapentane-5-sulfonate supplemented with 7% D_2O unless otherwise stated. The diamagnetic GaEnt complex with FepB was used for all holo NMR experiments, as Fe^{3+} is paramagnetic.

U-[^{13}C,^{15}N]^{1}H/^{2}H-labeled apo- (600 MHz) and holo-FepB (700 MHz) backbone and methyl group (600 MHz) chemical shift assignments were obtained from TROSY versions of three-dimensonal HNCA, HN(CO)CA, HNCACB, HN(CO)CACB, HN(CA)CO, and HNCO experiments (38–40) and a three-dimensional C-TOCSY-CHD$_2$ experiment, respectively (30).

NMR spin relaxation experiments for U-[^{15}N]^{1}H/^{2}H-labeled apo- and holo-FepB were conducted at a static magnetic field strength of 700 MHz using TROSY-modified experimental schemes (41). R_1 values were measured from two-dimensional spectra recorded with time (T) delays of 100, 170, 400 (twice), 680, 850, 1010, 1250, 1500 (twice), 1700, and 2000 ms. The R_2 values were measured from two-dimensional spectra recorded with T delays of 8 (twice), 16, 24, 32 (twice), 40, 48, 56, 64, and 80 ms. {^{1}H}^{15}N NOE experiments were recorded with and without a ^{1}H presaturation period of 5 s and an interscan delay of 5 s.

$^1D_{NH}$ residual dipolar couplings (RDC) were measured on partially aligned U-[^{15}N]^{1}H/^{2}H apo- and holo-FepB samples. The alignment media used included Pf1 phage (Asla Biotech Ltd.) at concentrations of 10 mg/ml and 12 mg/ml for holo- and apo-FepB, respectively (42). $^1D_{NH}$ RDCs were measured using an in-phase/anti-phase [^{1}H,^{15}N]HSQC experiment with 2048 × 512 complex points (43). A mixing time of 180 ms was used in the three-dimensional ^{15}N-edited NOESY-TROSY (44) and ^{13}C-edited NOESY-HMQC experiments. Additionally, a constant time, ^{13}C-edited NOESY-HSQC experiment with a 250-ms mixing time was measured by using a non-uniform sampling procedure (30%) and processed using MDDGUI 1.0 software (Arrowsmith Laboratory, University Health Network, University of Toronto), which requires MddNMR 2.0 (45). ILV-FepB was used for all NOESY measurements, and the ^{13}C-edited NOESY-HMQC was acquired in 99.9% D_2O.

Methyl Cross-saturation—Reverse methyl cross-saturation experiments were measured on a 0.4 mM sample of ILV-FepB in 50 mM sodium phosphate (pH 6.4) in 99.9% D_2O with and without GaEnt. Near complete exchange of residual $^1H^N$ with $^2H^N$ signals in apo-FepB was achieved by changing the buffer conditions to 50 mM sodium phosphate (pH ~8.0, 300 mM NaCl) and incubating the sample at 37 °C for 1–2 h. Apo-FepB was subsequently returned to its original buffer and room temperature conditions prior to complex formation with GaEnt. [^{1}H,^{13}C]HSQC experiments were performed as suggested (46, 47) with the irradiation radiofrequency field set at 5.5 ppm (4.0–7.0 ppm). The reference experiment was performed identically except with the irradiation set at −15 ppm, where there were no proton signals. Saturation of the protons of GaEnt was performed using 3.5-ms REBURP (48) pulses for a period of 1.5 s and an interscan delay of 2 s. The signal loss for each methyl group was calculated from the difference in signal intensity (I) between the experiment centered on 5.5 ppm and the reference, as follows: % signal loss = $[1 - (I_{5.5\text{ppm}}/I_{\text{reference}})] \times 100$.

Data Processing and Analysis—Absolute chemical shift changes upon ligand binding were examined on a per residue basis using a combined chemical shift difference according to Mulder *et al.* (49) for backbone (bb) and methyl groups: $\Delta\delta_{bb}$ (ppm) = $[\Delta\delta_{HN}{}^2 + (\Delta\delta_N/R_N)^2 + (\Delta\delta_{C'}/R_{C'})^2 + (\Delta\delta_C{}^\alpha/R_C{}^\alpha)^2 + (\Delta\delta_C{}^\beta/R_C{}^\beta)^2]^{1/2}$ and $\Delta\delta_{methyl}$ (ppm) = $[\Delta\delta_H{}^2 + (\Delta\delta_C{}^M/R_C{}^M)^2]^{1/2}$, where R_i denotes the scaling factor of nucleus i. The scaling factors used were $R_N = 6.4$, $R_{C'} = 3.0$, $R_C{}^\alpha$, $R_C{}^\beta = 3.2$, and $R_C{}^M = 5.4$.

Relaxation fitting data were extracted using the relaxation module in Sparky (50), and data fitting was performed by Curvefit version 1.4 (A. G. Palmer, Columbia University). {^{1}H}-^{15}N NOE values were determined from the experiments with and without irradiation. Data points with errors greater than 25% were excluded from the analysis. Relaxation data used in the rotational diffusion analysis were subject to filtering as described by Bax and co-workers (51). The rotational correlation time for the global tumbling (τ_m) for each residue was estimated from the R_2/R_1 ratio using the program R2R1_tm (A. G. Palmer, Columbia University), and the overall rotational correlation times (τ_c) for apo- and holo-FepB were determined by averaging the per residue τ_m values.

Structure Calculation—The mature FepB sequence (residues 24–315) was submitted to the ModWeb server for comparative structural model building, which relies on ModPipe (52) and generates models using MODELLER (53). A FepB homology model was built for all FepB residues using holo-ViuP (PDB code 3R5T) (54) as the template.

As input for structure calculations, deuterium isotope-corrected backbone chemical shifts (55, 56) were used to determine the position of secondary structure elements and dihedral backbone angle (Φ,Ψ) values, utilizing the programs CSI

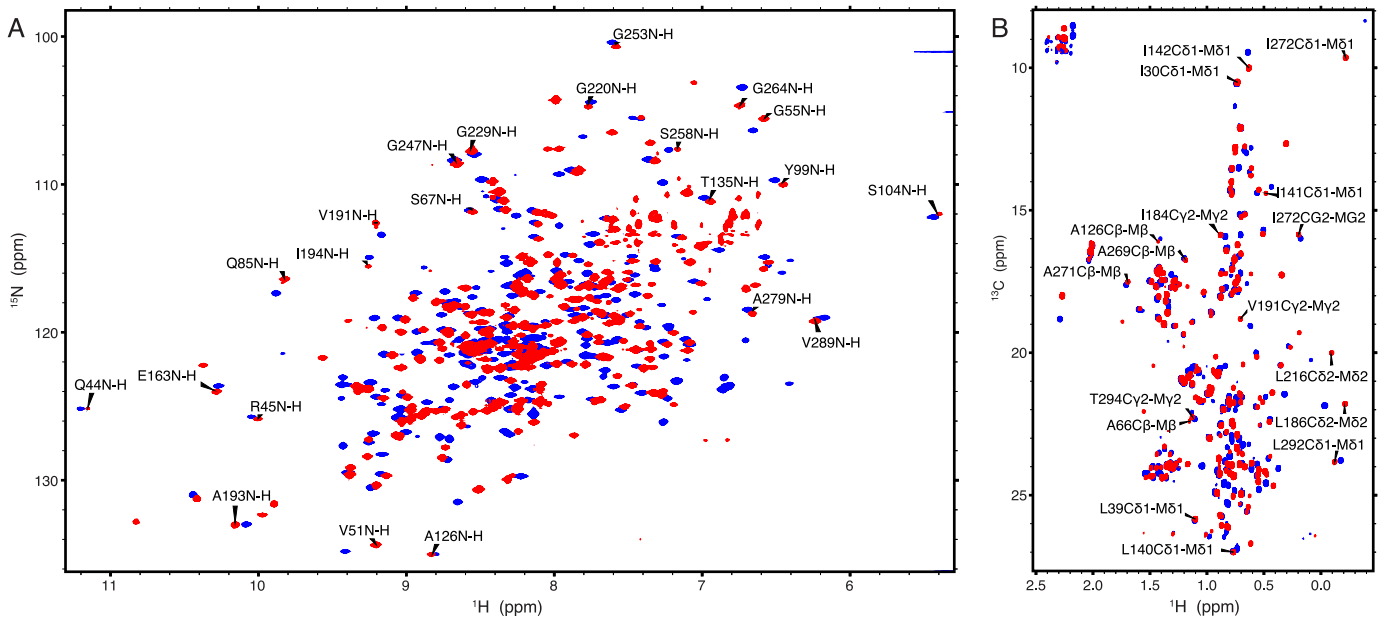

FIGURE 2. **NMR spectra of apo (*red*)- and holo-FepB (*blue*).** In *A*, overlaid U-[^{15}N]^{2}H/^{1}H-labeled apo- and holo-FepB (~1 mM) spectra from a ^{1}H-^{15}N TROSY-HSQC experiment. In *B*, overlaid U-[^{13}C,^{15}N]^{2}H/^{1}H-labeled apo- and holo-FepB (~1 mM) spectra from a CHD_2-detected CT-[^{1}H-^{13}C]HSQC experiment. All experiments were acquired in 50 mM Na_3PO_4 (pH 6.4) at 298 K on a 700 MHz (^{1}H-^{15}N TROSY-HSQC) or 600 MHz (CT-[^{1}H-^{13}C]HSQC) NMR spectrometer. Several residues that could be clearly labeled and with adjacent apo- and holo-peaks are indicated.

(Chemical Shift Index) (57) and TALOS+ (58), respectively. α-Helical secondary structure elements were implemented in structure calculations using artificial hydrogen bond restraints according to Tugarinov *et al.* (59). Similarly, artificial β-sheet hydrogen bond restraints based on the holo-ViuP (PDB code 3R5T) structure were employed conservatively in structure calculations. Dihedral (58) and RDC (60, 61) restraints and NOESY distance restraints were used as input for structure calculations. Structures were calculated using torsion angle-simulated annealing in the program Xplor-NIH (62) according to a two-step, low temperature protocol (47, 63–65) wherein an ensemble of the 30 lowest energy structures is generated and validated using PSVS (Protein Structure Validation Software suite) (66).

Homology Modeling of FepCD—A homology model for FepCD was constructed by threading its sequence onto the BtuCD structure (PDB code 2QI9) using MODELLER (52). Two FepD chains were modeled using the BtuC homodimer (34.8% sequence identity) as the template.

Accession Numbers—NMR backbone chemical shift assignments for apo- and holo-FepB have been deposited in the Biological Magnetic Resonance Data Bank (BMRB) under accession code 19143. The atomic coordinates for the 30 lowest energy structure ensembles of apo- and holo-FepB have been deposited in the Protein Data Bank under accession codes 2M6K and 2M6L, respectively.

RESULTS

NMR Characterization—We report here the solution structures of apo- and holo-FepB (34 kDa). These NMR structures represent a significant milestone in PBP studies, as these are the first solution structures of a type III PBP among a myriad of existing crystal structures (12). The holo-FepB protein was solved in the presence of the diamagnetic siderophore $[Ga^{III}(Ent)]^{3-}$ (GaEnt) as a substitute for paramagnetic FeEnt. It is important to note that Ga^{3+} has the same charge and similar properties as Fe^{3+} (67), and it has previously been used as a substitute for FeEnt in NMR studies of the FepA cork domain (68, 69).

The study of PBPs by NMR poses a significant challenge, as their larger size (~25–70 kDa) (12) requires specialized isotope-labeling schemes and NMR pulse programs to acquire high quality spectra. The combined use of deuteration and TROSY NMR experiments allowed us to determine a nearly complete assignment of the $^{1}H^{N}$, ^{15}N, $^{13}C'$, $^{13}C^{\alpha}$, and $^{13}C^{\beta}$ chemical shifts for apo- (95%) and holo-FepB (96%) (Fig. 2). Furthermore, a high percentage of possible methyl group assignments for Leu (82%), Val (91%), and Ile (94%) was determined using our previously reported CHD_2 methyl assignment method (30). In total, 103 methyl groups could be assigned for holo-FepB compared with 110 for apo-FepB. Overall, the residues that could not be fully assigned or were missing include residues 1–13 (His tag), 46–47, 57–60, 115–118, 140–142, and 159–160. These residues could not be observed in either the apo- or holo-system, suggesting that the absence of signal is not correlated with ligand binding.

The solution structures of apo- and holo-FepB were determined first by analyzing the secondary structure from the backbone chemical shifts. Subsequently the three-dimensional solution structures were determined using a two-stage, low temperature, simulated annealing protocol (63) and a starting homology model based on holo-ViuP (PDB code 3R5T; 35% sequence identity). The ^{15}N- and ^{13}C-edited NOESY experiments generated 1097 and 1003 upper distance restraints for apo- and holo-FepB, respectively. Although these restraints were distributed throughout the protein sequence, more NOEs were observed for the C-terminal lobe (residues 184–315; data

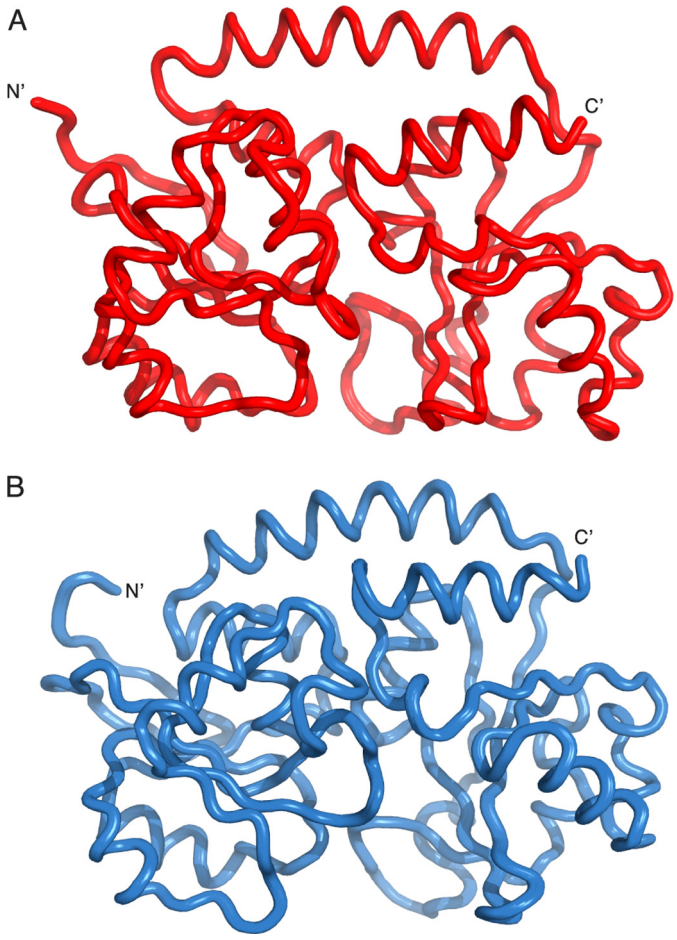

FIGURE 3. **The 30 lowest energy NMR structures for apo- (*A*) and holo-FepB (*B*), depicted in *red* and *blue*, respectively.** The two-stage low temperature simulated annealing protocol employed in the structure calculations allows for all 30 structures to converge within ~0.1 Å (Table 1).

TABLE 1
Experimental restraints and structural statistics for the 30 lowest energy structures for apo- and holo-FepB

	Apo	Holo
Number of experimental restraints		
Upper distance restraints from NOE		
Total	1097	1003
Short/medium range	726	588
Long range	371	415
^{1}DNH RDCs	187	210
Dihedral angle restraints (TALOS+)	469	464
Hydrogen bonding restraints	132	124
Average r.m.s.d. values from experimental data		
Distance restraint violation (Å)	0.071	0.077
Dihedral angle restraint violation (°)	0.156	0.356
RDC restraint violation (Hz)	0.094	0.102
Average r.m.s.d. values from idealized covalent geometry		
Bonds (Å)	0.003	0.003
Angles (°)	0.426	0.449
Impropers (°)	0.403	0.407
PROCHECK Ramachandran analysis (folded regions (%))		
Residues in most favored regions	79.7	82.2
Residues in additional allowed regions	16.6	14
Residues in generously allowed regions	3.7	1.9
Residues in disallowed regions	0	1.9
Coordinate precision of folded regions		
Backbone (Å)	0.08 ± 0.02	0.09 ± 0.05
All heavy atoms (Å)	0.09 ± 0.02	0.12 ± 0.04

not shown). To determine accurate helix and domain orientations, backbone H-N RDC restraints were employed in the Xplor-NIH structure refinement protocol. RDCs were successfully measured for 187 (~64%) and 210 (~72%) residues for apo- and holo-FepB, respectively. The backbone heavy atom r.m.s.d. for the well folded region of FepB (residues 24–315) from the 30 lowest energy structures was 0.08 ± 0.02 Å (apo) and 0.09 ± 0.05 Å (holo) (Fig. 3). PROCHECK Ramachandran plots revealed that 79.7% (apo) and 82.2% (holo) of the residues were in the most favored regions, whereas 1.9% of holo residues were in the disallowed regions. A summary of the structure calculation statistics can be found in Table 1.

Changes to secondary structure elements upon ligand binding were evaluated with the neighbor-corrected structural propensity calculator (ncSPC) using backbone chemical shifts as input (70, 71). The overall topology of apo- and holo-FepB is a mixed α/β type consisting of 10 α-helices and 12 β-strands, where each domain has a central 5-stranded β-sheet (Fig. 4, *A*–*C*). This is in good agreement with other type III PBPs, which are composed of two globular domains of mixed α/β elements (Rossmann fold) and an interdomain α-helix. In the structures of apo- and holo-FepB, the α-helices are well structured, whereas the β-stands are not as well defined, with some represented as extended elements (Fig. 3). The loss of representation for β-strands and -sheets is due to the use of perdeuteration, which leads to the loss of proximal H^{α} proton NOE information in the β-sheets. Pairwise structural alignment of apo- and holo-FepB reveals an r.m.s.d. of 2.96 Å (Fig. 5*A*). This large value can in part be attributed to the poor resolution of the β-strands of the two main β-sheets. A decrease in the binding pocket solvent-accessible surface area (SASA) of 32.85 Å^2 (Table 2) suggests that FepB experiences structural changes in the presence of ligand, which could also contribute to the high r.m.s.d. The binding of GaEnt does not appear to have a great effect on the contact area (0.44% increase) between the amino (N)- and carboxyl (C)-terminal lobes (Table 2) or the overall fold of the protein. However, some notable changes are observed in three regions: residues 70–94, 227–242 (loop), and 294–302 (loop). Residues 70–94 comprise a ~12 residue loop followed by an α-helix that moves significantly upon ligand binding (Fig. 5*B*). This movement positions residues 70–76 between the two lobes and proximal to the putative binding pocket of holo-FepB. Based on ncSPC scores, residues 227–242 and 294–302 are expected to become more and less extended, respectively, upon ligand binding (Fig. 4*D*). Region 227–242 undergoes a significant structural change leading to a ~4.6 Å tilting movement of Arg-239 and neighboring residues into the GaEnt binding pocket (Fig. 5*C*). Interestingly, in apo-FepB the side chains of Phe-297 and Arg-298 from the 294–302 loop are located near the mouth of the binding pocket, but in holo-FepB these residues are rotated into the interdomain cleft region (Fig. 5*D*). It appears that the movement of this loop contributes to the formation of the GaEnt binding pocket.

Ligand Binding—FepB was shown previously to bind FeEnt with K_d ~135 nM and K_d ~30 nM by gel filtration chromatography and fluorescence spectroscopy, respectively (72). Binding of GaEnt and FeEnt to FepB occurs with similar affinity (K_d, GaEnt = 162 ± 4 nM; K_d, FeEnt 169 ± 5 nM; Fig. 6*A*) as mea-

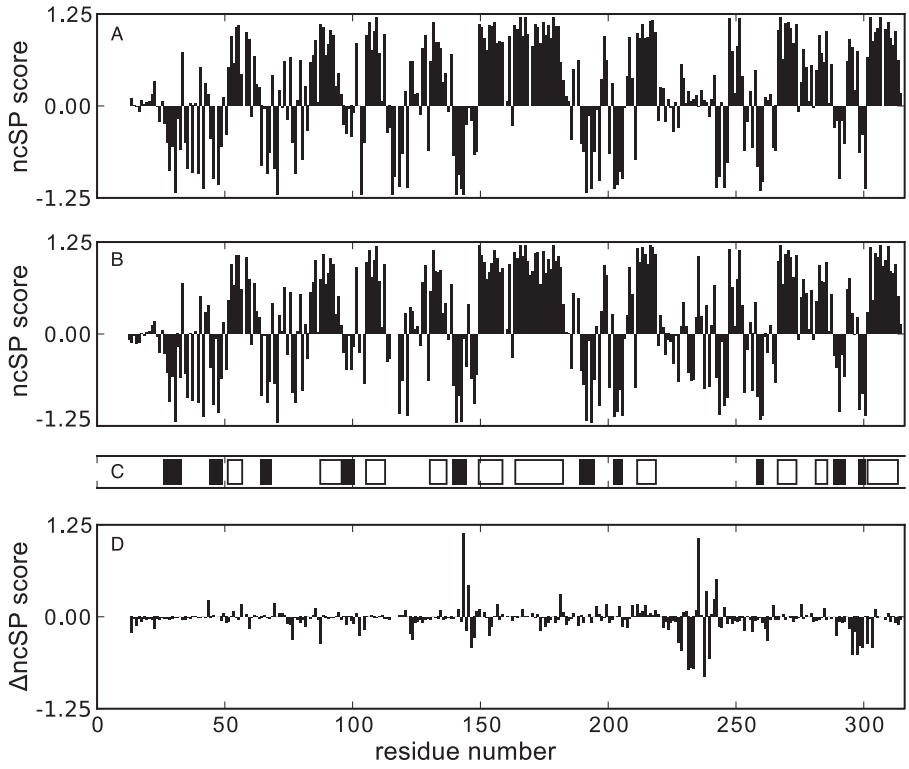

FIGURE 4. **The consensus ncSP scores for apo- (*A*) and holo-FepB (*B*), the overall consensus topology of FepB based on apo- and holo-FepB ncSP scores (where α-helices are □ and β-strands are ■) (*C*), and the difference (holo-apo) in values for FepB chemical shifts (*D*).** Positive ncSP values indicate α-helical content, negative values indicate the presence of β-strands or an extended structure, and 0 values are expected for random coil.

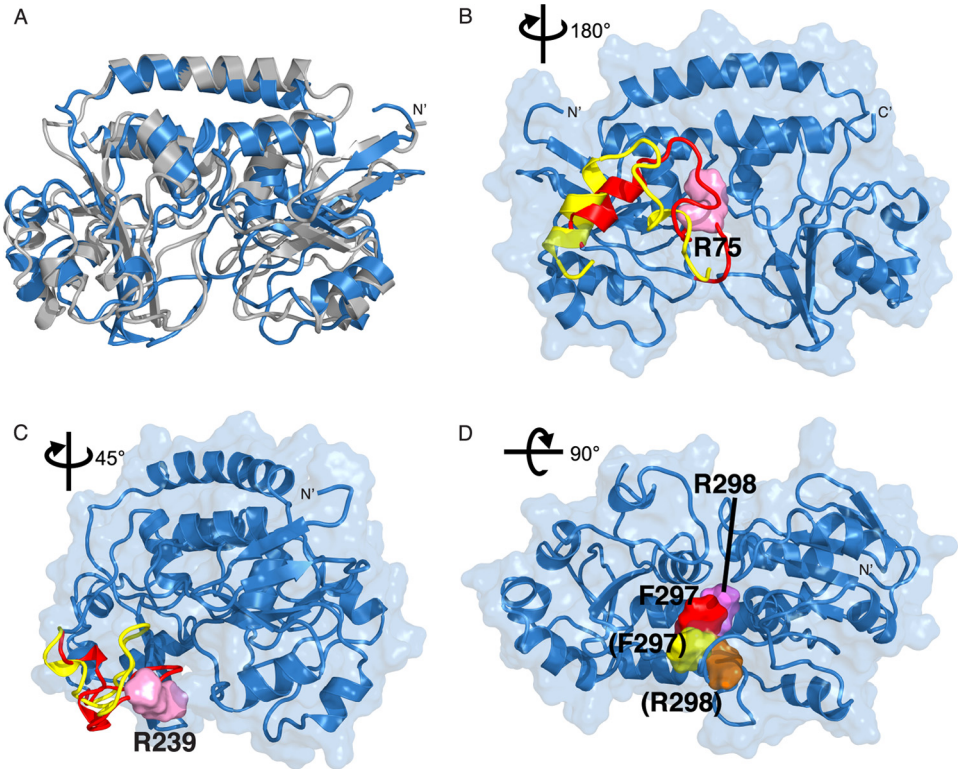

FIGURE 5. **Structures of apo- (*gray*) and holo-FepB (*blue*) with specific structural differences compared.** *A*, structural alignment of residues 25–315 of the lowest energy apo- (*gray*) and holo-FepB (*blue*) structures (r.m.s.d. 2.96 Å). For *B–D*, only the loop residues of apo-FepB (*yellow*) are displayed, and for holo-FepB, *highlighted* residues are shown in *red* with remaining residues shown in *blue*. *B*, the loop residues 70–94 of apo- and holo-FepB. These residues point into the binding pocket in the holo-FepB structure, with Arg-75 represented by a *pink space-filled form*. *C*, movement of the loop residues 227–242 in the apo- and holo-FepB structures with Arg-239 represented in *pink* and *space-filled form*. *D*, movement of loop residues 294–302 helps to position Phe-297 and Arg-298 in the binding pocket. Phe-297 and Arg-298 are represented in *space-filled form* with their apo- and holo-FepB positions indicated with and without *parentheses*, respectively.

TABLE 2

Comparison of type III PBP structures

Changes in interlobe and binding pocket SASA upon ligand binding were calculated using Contact Map Analysis (83) and CASTp (93), respectively. Structural alignment of apo- and holo-PBP forms were calculated using PDBeFold (86).

PBP	Form	PDB ID	$\Delta_{holo\text{-}apo}$ interlobe contact SASA	$\Delta_{holo\text{-}apo}$ binding pocket SASA	Holo-Apo structural alignment	N-lobe holo-apo alignment	C-lobe holo-apo alignment
			%	$Å^2$	*r.m.s.d.*	*r.m.s.d.*	*r.m.s.d.*
FepB	Apo	2M6K					
	Holo	2M6L	0.44	−32.85	2.96	2.69	2.39
ViuP	Apo	3R5S					
	Holo	3R5T	36.67	−21.07	1.78	0.30	0.41
HtsA[a]	Apo	3EIW					
	Holo-open	3LHS	1.26	−104.05	0.18	0.07	0.10
	Holo-closed	3LI2	21.31	−4.39	0.97	0.30	0.50
SirA	Apo	3MWG					
	Holo	3MWF	10.43	−39.15	0.84	0.21	0.61
FeuA	Apo	2WI8					
	Holo	2WHY	29.53	−50.07	1.93	0.35	0.39
FhuD[b]	Apo						
	Holo	1EFD	2.43	−3.77	0.84	0.49	0.36
BtuF	Apo	1N4D					
	Apo-complex[c]	2QI9					
	Holo	1N4A	−3.22,5.12[c]	23.26, 237.17[c]	0.89,1.58[c]	0.34,0.27[c]	0.45,0.39[c]
Hmut	Apo	3MD9					
	Holo	3NU1	2.22	−28.54	1.31	0.22	0.51

[a] Holo-HtsA has two crystal forms: an open (3LHS) and a closed (3LI2) conformation.
[b] The apo-FhuD structure was provided by Dr. Karla D. Krewulak (94).
[c] Apo-complex BtuF was extracted from the complex with its ABC transporter BtuCD (2QI9).

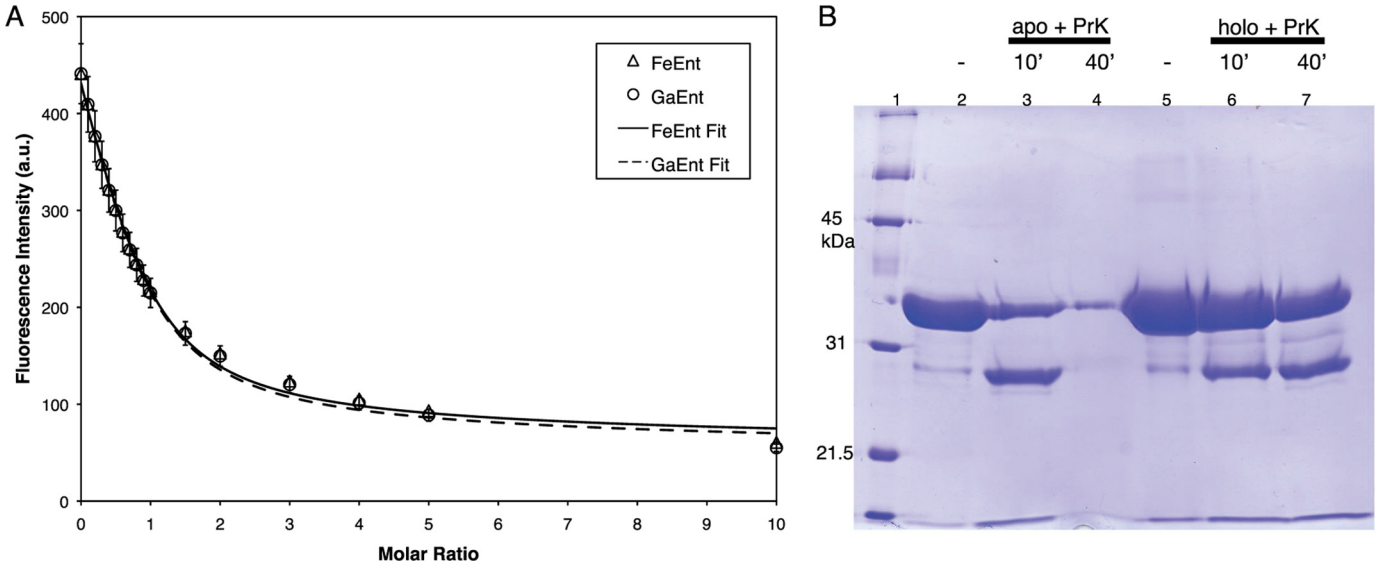

FIGURE 6. **FeEnt and GaEnt binding properties of FepB.** *A*, fluorescence spectroscopy titration of FepB with FeEnt and GaEnt. The fluorescence intensity in arbitrary units (*a.u.*) at 330 nm decreases upon the addition of ligand. Each addition of GaEnt (○) and FeEnt (△) is shown. The curve fits for the determination of K_D are also depicted. All experiments were performed in triplicate. *B*, proteinase K protection assays of FepB with and without GaEnt were run on a 12% SDS-PAGE. Identical results were also obtained with the FeEnt-FepB complex (data not shown). *Lane 1*, low range molecular weight markers; *Lanes 2* and *5*, controls for FepB and GaEnt-FepB without proteinase K (*PrK*). *Lanes 3* and *4*, FepB after 10 and 40 min of proteinase K digestion, respectively. Similarly, *lanes 6* and *7* are GaEnt-FepB after 10 and 40 min of digestion, respectively.

sured by fluorescence spectroscopy. FepB ligand binding was also assessed using proteinase K digestion assays. In the absence of ligand, FepB is rapidly degraded by proteinase K, but in complex with GaEnt or FeEnt, FepB is protected to similar levels (Fig. 6*B*). In addition, ^{1}H-^{15}N TROSY HSQC experiments of FepB complexed with FeEnt or GaEnt show similar peak patterns. However, the presence of ferric iron in the FeEnt-FepB sample results in the broadening of backbone amide resonances for residues close to the ligand binding site (data not shown).

Binding of GaEnt to FepB was also examined from observed NMR chemical shift perturbations (CSP, shown in Fig. 7). From the combined backbone CSP, there are significant changes distributed throughout the protein sequence starting at residue 50. Mapping of the backbone CSPs onto the holo-FepB structure reveals that the affected regions are the long interdomain α-helix and regions proximal to the interdomain cleft (Fig. 7*A*). Moderate methyl CSPs are distributed throughout the C-lobe β-sheet, and large methyl CSP values are found for residues leading into (Ala-232) and exiting (Ile-243) the loop region 227–242 (Fig. 7*B*), which also undergoes significant conformational changes upon GaEnt binding.

Methyl Cross-saturation—NMR cross-saturation experiments are an indispensable tool for examining the interface of protein-protein interaction complexes (73). The CSP is an effective technique for monitoring residues involved in ligand binding (or complex formation). However, the interpretation of

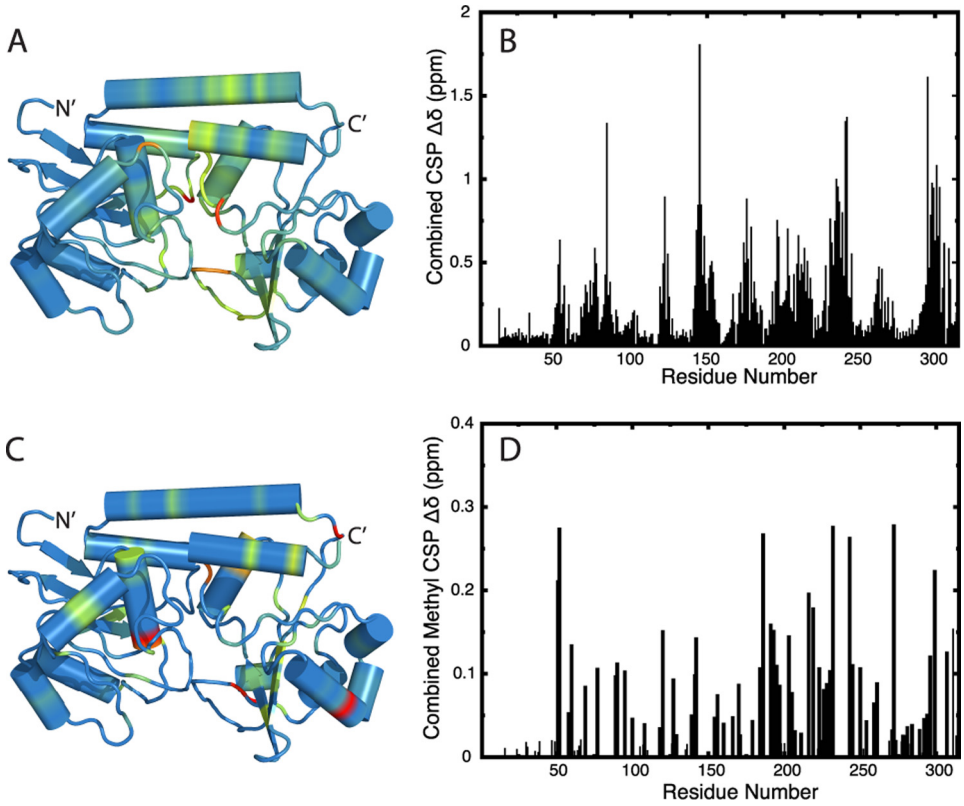

FIGURE 7. **CSP analysis of GaEnt binding to FepB.** Mapping of consensus backbone (*A*) and methyl (*C*) CSPs plotted on the lowest energy holo-FepB structure, where helices are represented as *cylinders*. The color gradient of *blue* to *red* indicates regions experiencing the least to greatest CSP, respectively. For backbone CSPs, regions near the binding pocket and the interdomain helix are notably affected, whereas for methyl CSPs, β-strand elements in the C-lobe and methyl groups belonging to the flexible loop (residues 225–250) are affected. Data for backbone and methyl CSPs can be found in *B* and *D*, respectively.

these values can be difficult when the protein experiences substantial conformational changes upon interaction, leading to large CSP values distributed throughout the protein rather than local effects (74). Amide or methyl cross-saturation experiments are often performed to closely examine the interface where complex formation occurs and can complement CSP analysis. Methyl cross-saturation methods were performed using specifically labeled Ile(δ1), Leu, and Val methyl groups, which simplifies the NMR spectra and provides better resolution for large proteins, higher sensitivity due to narrow line widths, and improved magnetization transfer efficiency (46). In addition, methyl groups are excellent reporters of hydrophobic interactions that often make significant thermodynamic contributions to the formation of protein-protein complexes. In this study, we employed the "reverse methyl cross-saturation" technique in which the smaller interacting partner is selectively irradiated and magnetization is transferred to isotopically labeled methyl groups of the larger protein (47, 74, 75). In our case we made two modifications to the published experiment. First, instead of using a reference spectrum without irradiation (T_{sat} = 0 s) we employed the same T_{sat} = 1.5 s in both the reference and irradiation experiment to ensure the only difference in the experiments was the location of the radiofrequency pulse. Second, we targeted the small, non-ribosomally synthesized ligand, Ent (669 Da), for irradiation and detected its interface with a large protein (FepB, ~34 kDa). Enterobactin is composed of three 2,3-catecholate moieties linked to a triserine backbone, and the proton signals of GaEnt have reported chemical shifts in the region between ~3.7 and 7 ppm (76, 77). Specifically ILV methyl-protonated and otherwise deuterated holo-FepB was dissolved in ~100% D_2O, and no ^1H signals originating from the protein were observed in the irradiated region (4–7 ppm). However, because of incomplete H/D exchange, 15 backbone $^1H^N$ signals remained visible near 8 ppm; but these signals did not interfere with the cross-saturation experiment. A control experiment performed with apo-FepB revealed that a background signal loss of ~5% can be expected (Fig. 8*A*), and residues that experienced signal loss greater than 5% were considered significantly affected. In the holo-FepB experiment, magnetization was expected to transfer from GaEnt by spin diffusion to the selectively protonated methyl groups of FepB involved in ligand binding. Signal loss was below 5% for the majority of the protein residues, indicating that they were not affected by ligand binding (*cf.* control experiment for apo-FepB). Resonances V51Cγ1, V51Cγ2, V195Cγ1, and I242Cδ1, however, experienced a significant reduction in signal intensity of ~47, 8, 31, and 32%, respectively (Fig. 8*A*). Mapping of the affected residues onto the lowest energy holo-FepB structure revealed that all three residues were found within the cleft region between the N- and C-terminal domains (Fig. 8*B*). In agreement with the backbone and methyl CSP results, the regions surrounding Val-51 and Ile-242 experienced significant changes to their chemical environment upon ligand binding. In particular, Val-51/Thr-52 show the largest combined methyl CSP in the N-terminal portion of

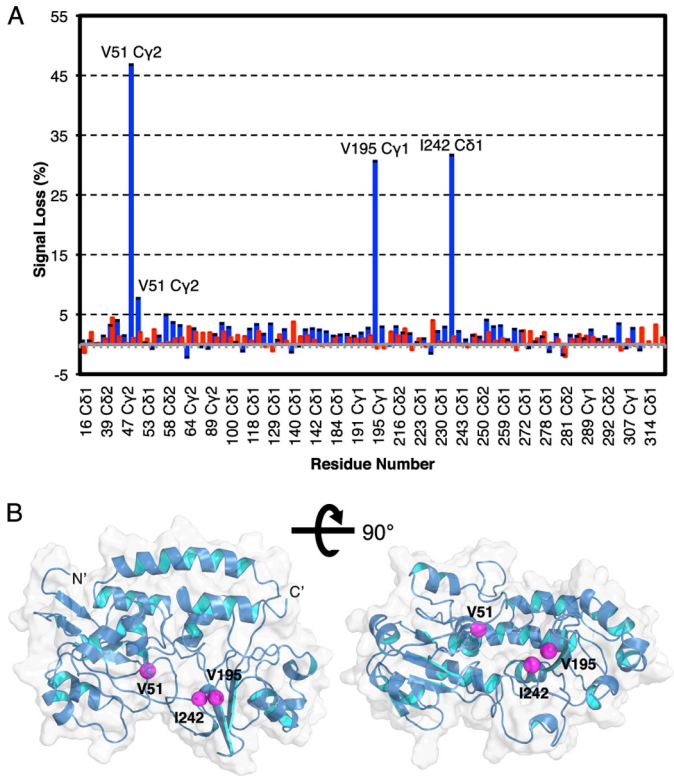

FIGURE 8. **Reverse methyl cross-saturation experiment of the GaEnt-FepB complex.** *A*, percentage of lost signal intensity of the methyl groups in apo-FepB (*red*) and FepB complexed with GaEnt (*blue*), with selective irradiation set at −15 ppm (reference) and 5.5 ppm (experiment). Based on the results of the apo-FepB experiment, residues experiencing <5% signal loss were deemed not significantly affected; affected residues in the holo-FepB experiment are labeled for clarity. *B*, the affected methyl signals are shown on the lowest energy holo-FepB (*blue*) structure as *pink spheres*, representing the methyl $C^{\gamma/\delta}$ position. When holo-FepB is rotated about the *x* axis by 90°, the proximity of the affected methyl signals to the putative Ga/FeEnt binding pocket can be clearly seen.

FepB, and Asp-241/Ile-242 have significant backbone CSP values.

FepB Dynamics—Backbone ^{15}N relaxation measurements to examine fast (ps to ns) time scale backbone dynamics were performed on apo- and holo-FepB (Fig. 9). Overall, apo-FepB appears well ordered (*i.e.* high NOE and uniform R_1 and R_2 values) with the exception of the highly flexible N-terminal His tag (residues 13–23) and residues within a loop region (residues 225–242). For this loop, residues 228–230, 233–234, and 236–240 are significantly more rigid in the holoprotein (Fig. 9*C*). Moreover, this increased order affects residues neighboring Ile-242, which was identified by methyl cross-saturation as an interface residue with GaEnt. Additionally, Ala-232, Asp-241, Ile-242, and Ile-243 experienced significant CSPs. Two other regions, residues 77–81 and 293–303, also appear to be more dynamic in apo-FepB than holo-FepB, although there is a higher degree of uncertainty for the apo-FepB $\{^1H\}$-^{15}N NOE values for these residues. These two regions also undergo conformational changes in the transition from apo- to holo- FepB and appear to have a role in ligand binding.

To examine whether the rotational correlation time (τ_c) is changed upon ligand binding, we performed rotational diffusion analysis. It was found that the average times for apo- and holo-FepB were 23.2 ± 2.2 and 19.7 ± 1.7 ns, respectively, which are in accordance with expected values for a globular monomeric protein of ~34 kDa. The hydrodynamic radius (r_H) for apo- and holo-FepB was determined from their respective lowest energy ensemble structures using the program HYDROPRO (78). Similar, to the τ_c results, apo-FepB was found to have a slightly larger r_H value (2.10 ± 0.01 nm) compared with holo-FepB (2.08 ± 0.01 nm). The differences in the τ_c and r_H values for apo- and holo-FepB are not significant but suggest that holo-FepB is more compact than apo-FepB.

Furthermore, we analyzed whether the individual N- and C-terminal domain lobes of apo- and holo-FepB tumble independently in solution. No significant change in correlation time (data not shown) was observed when the lobes were treated independently, indicating that the lobes move together in solution.

FepCD Homology Modeling—A homology model of the inner membrane ABC transporter FepCD was constructed to compare the periplasmic surface of FepD and BtuC. Arg-60 in both of the FepD homodimer chains is in a homologous position to Arg-56 from both BtuC homodimer chains, shown previously to be important for interactions with BtuF (79). A comparison of the BtuC loop, which interacts with BtuF, and a similarly positioned FepD surface loop revealed differences in the electrostatic composition (Fig. 10). In BtuC, the loops are composed of both basic and acidic amino acids, whereas in FepD the purported FepB-interacting loop is primarily acidic (Fig. 10).

DISCUSSION

In this study, NMR spin relaxation experiments were used to evaluate changes in FepB dynamics in the presence and absence of ligand. This is particularly relevant for PBPs, as opening and closing motions are important for both ligand binding and release (Fig. 1). For type I and II PBPs, it has been suggested that the rigidity of the hinge region, which is strongly influenced by the hydrogen bonding network between hinge elements, becomes more ordered upon ligand binding leading to large scale opening-closing motions (80). In contrast, for type III PBPs, the hydrogen-bonding network afforded by the ~20-residue α-helix that connects the N- and C-terminal lobes is typically not affected by ligand binding and is thought to sterically limit any large scale opening and closing motions. These movements originate from minor changes (*e.g.* a slight bend) in the interdomain α-helix or at residues entering or exiting this helix (Fig. 11). Changes to the interdomain α-helix were also observed for holo-FepB, which shows a more pronounced bend in the first part of its interdomain α-helix compared with the apo form. This results in a minor displacement of the N-lobe toward the C-lobe but does not lead to any significant domain-closing motions. Moreover, submission of the lowest energy apo- and holo-FepB structures to the Dyndom server (81) did not reveal any dynamic hinge-bending domain motions associated with ligand binding.

PBPs also experience changes to the interface between their two lobes upon ligand binding. In types I (*e.g.* maltodextrin-binding protein) (15) and II (*e.g.* Ile/Leu/Val-binding protein) (82) the apo forms are characterized by a near absence of interlobe contacts at the binding pocket, whereas the holo forms show an increase in the number of interlobe

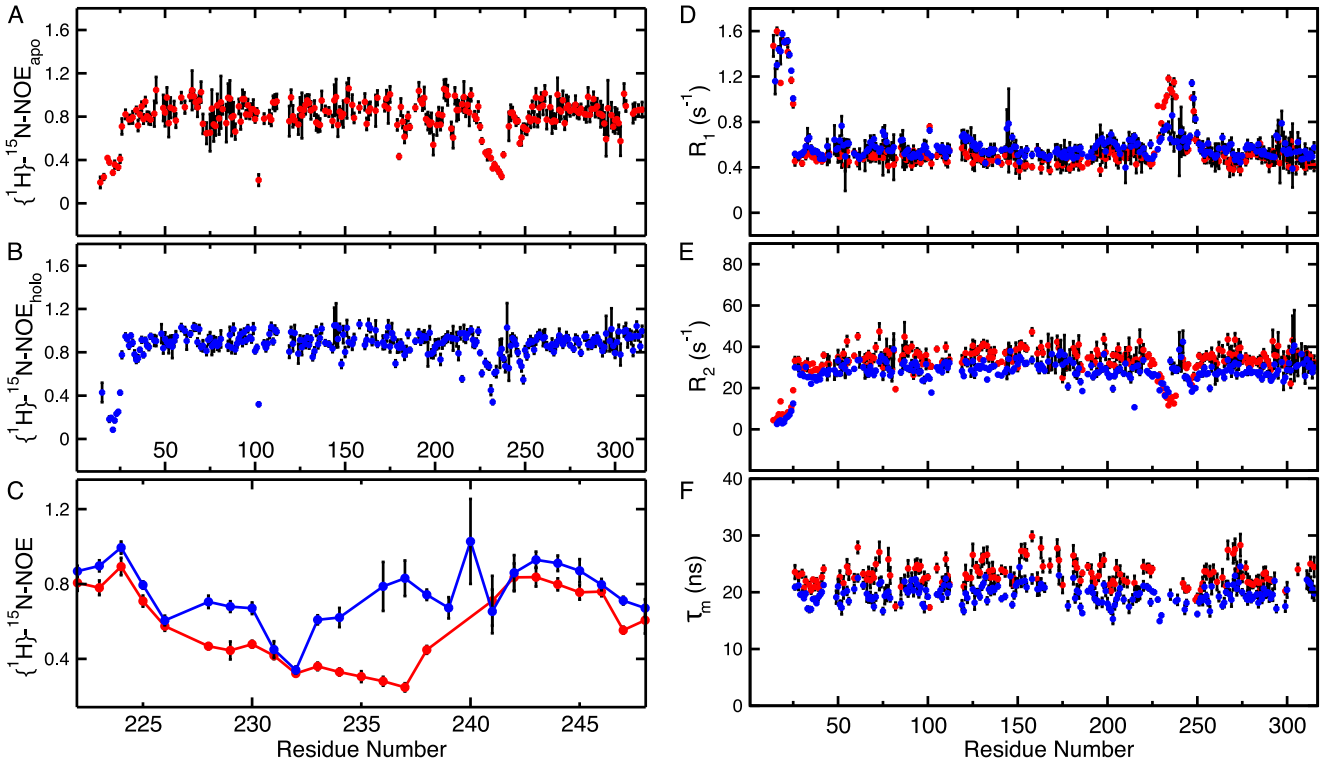

FIGURE 9. **NMR dynamics analysis of apo- (*red*) and holo-FepB (*blue*).** *A* and *B*, $\{^1H\}$-^{15}N NOE relaxation data for apo- (*A*) and holo-FepB (*B*). In *C*, residues 225–250 in the large loop region, which shows the greatest difference in heteronuclear NOE values between apo- and holo-FepB forms, are *highlighted*. In particular residues 233–242 are less flexible in holo-FepB. Standard deviations of heteronuclear NOE values are indicated. *D* and *E*, ^{15}N R_1 (*D*) and R_2 (*E*) relaxation data for apo- and holo-FepB. In *F*, the correlation time of global tumbling (τ_m) is calculated from the R_2/R_1 ratio. Apo- and holo-FepB data were recorded at a static magnetic field strength of 16.4 Tesla.

interactions, which help to stabilize the closed ligand bound state. In contrast, both the apo and holo forms of type III PBPs have extensive interlobe contacts, and ligand binding appears to produce subtle rearrangements to this interface. Structural differences that arise from changes to the intermolecular interactions at this region were evaluated by assessing the interlobe SASA (Table 2) (83). Small differences in the interlobe contact surface between apo and holo forms of type III PBPs were observed for FepB, SirA, FhuD, BtuF, and HmuT, whereas for ViuP, HtsA, and FeuA the closed holo conformation shows an increase in contact area between the lobes. Changes to the interlobe interface during the transition between apo and holo forms appears to be important in some type III PBPs for accommodating the structural changes associated with ligand binding, and they could have a role in regulating the opening-closing domain motions. Interestingly, apo-BtuF extracted from the complex with its ABC transporter (BtuCD) experiences a decrease in interlobe SASA, indicating that its lobes are spread further apart in complex with the transporter than the isolated apo form.

The binding of GaEnt to FepB reveals a reduction in the binding pocket SASA that is consistent with other related type III PBPs (Table 2). The notable exception is BtuF, which (20) experiences an expansion of its binding pocket upon cyanocobalamin interaction (Table 2). An increase or reduction in binding pocket SASA is related to the size of the ligand, the depth of binding, and structural features of the protein. For example, in type III PBPs that bind small ions (*e.g.* TroA and Zn^{2+} (PDB code 1TOA)) the ligand is bound in a completely occluded manner, whereas for PBPs that bind larger siderophores (*e.g.* FhuD and gallichrome (PDB code 1EFD)) the ligand is usually solvent-exposed (12).

Determination of the FepB solution structures relied on recent advancements in NMR technology that facilitated our ability to solve protein structures with a molecular mass of >25 kDa. The introduction of labeled Ile(δ1), Leu, and Val methyl probes into a deuterated FepB background (34) and cost-effective methyl assignment techniques (30) allowed us to acquire the distance information required to converge the global folds of this protein. A hallmark of type III PBPs is their low primary sequence identity and high structural similarity (84). Submission of apo- and holo-FepB to the DALI server (85) revealed a structural similarity to the type III PBPs ViuP (3.3/3.2 Å r.m.s.d. for apo-/holo-FepB, respectively) and HtsA (3.4/3.3 Å r.m.s.d. for apo-/holo-FepB). In addition, a comparison of secondary structure element positions for the apo and holo forms of ViuP with FepB reveal a match of 85 and 80% (86), respectively, despite the poorly defined β-sheets in FepB. The crystal structures for ViuP were only recently reported (54), and this PBP binds the catecholate-type siderophore ferric vibriobactin (FeVib; $[Fe^{III}(Vib)]^{2-}$). FeVib has a 2- charge and coordinates iron with five ligands from its catecholate groups, whereas FeEnt has a 3-charge and provides six hard ligands to Fe^{3+} (87). Typically, type III PBPs that bind catecholate-type siderophores (CeuE (88), YclQ (89), and FeuA (12, 21)) use three basic residues to neutralize the 3- charge of their siderophores. However, ViuP uses only two (Arg-244 and Arg-297) due to the

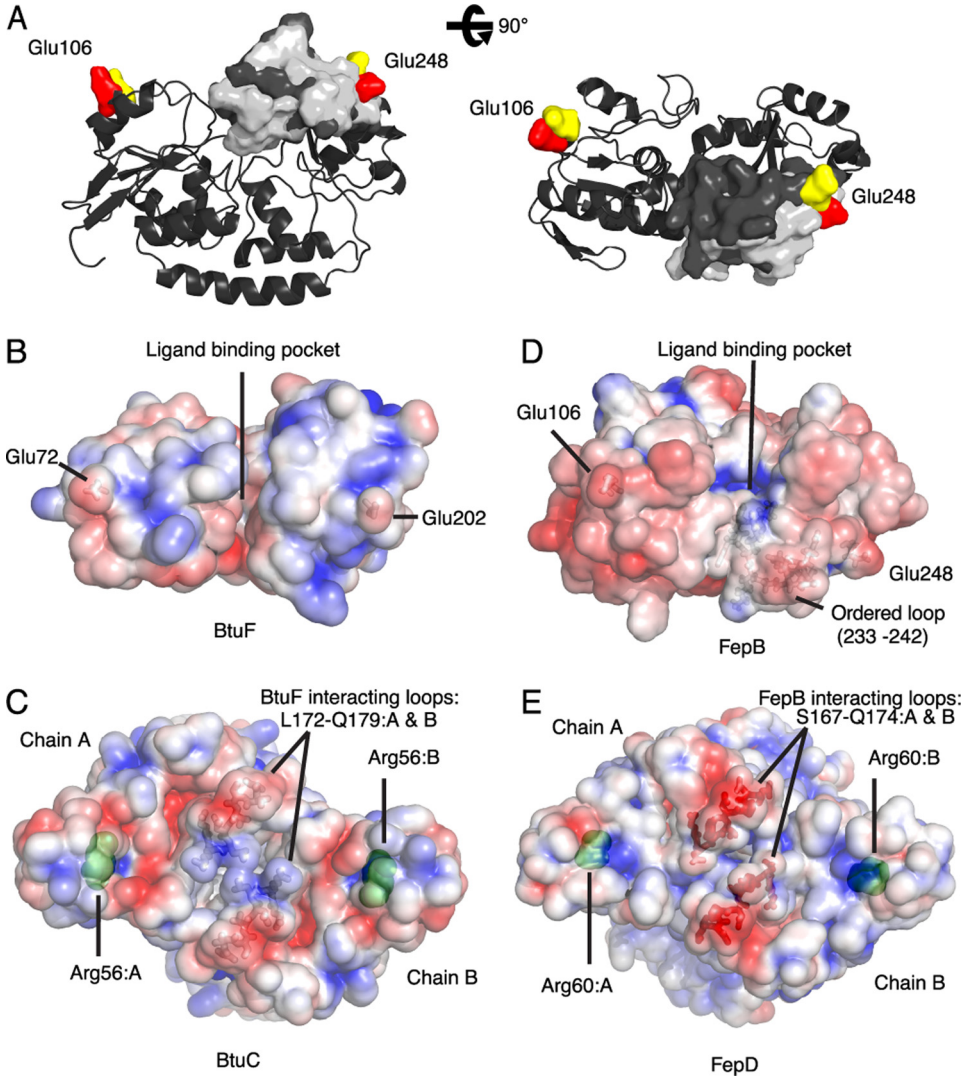

FIGURE 10. **Examination of regions involved in FepB interaction with its cytoplasmic membrane ABC transporter, FepCD.** In *A*, conserved Glu residues 106 and 248 positions are shown for apo- (*yellow*) and holo-FepB (*red*) on the holo-FepB structure. A *space-filling* format is used to represent the conserved Glu residues and the flexible loop region (residues 225–242) of apo- (*white*) and holo-FepB (*dark gray*). *B* and *C*, electrostatic contour plots of BtuF (*B*) and BtuC (*C*) looking at the interaction sites. *D* and *E*, electrostatic contour plots of FepB (*D*) and the FepD homology model (*E*). For the electrostatic plots of BtuF (*B*) and FepB (*D*), the perspective is looking up from the transporter, and for BtuC (*C*) and FepD (*E*) the view is looking down from the periplasm. Electrostatic plots are scaled ±3 *kT/e*, where the positive regions are shown in *blue*, and negative regions are *red*.

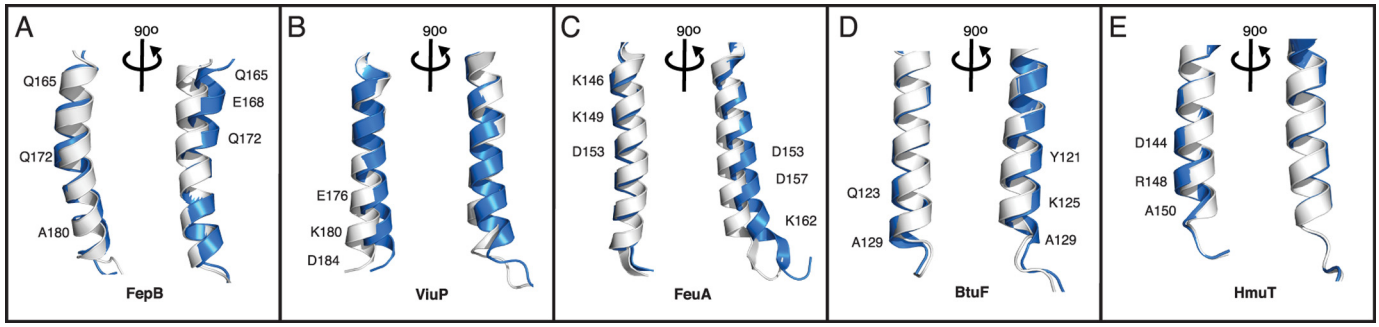

FIGURE 11. **Structural comparison of the interdomain α-helices of type III PBPs.** Examination of apo (*gray*) and holo (*blue*) forms of FepB (*A*), ViuP (*B*), FeuA (*C*), BtuF (*D*), and HmuT (*E*). Of note, the left perspective is looking top-down on the interdomain α-helix, whereas the rotated view (90° about the *y* axis) gives a side-on profile. The N-lobe of both forms of each protein was aligned prior to analysis. Interdomain α-helix residues for which positions were affected by the apo-to-holo transition are labeled.

2-charge of FeVib. A structure-based sequence alignment reveals that FepB R298 aligns with Arg-297 of ViuP and is positioned in the binding cavity, indicating that it has a similar role in Ga/FeEnt coordination (Fig. 12). Arg-239 of holo-FepB sits in the binding pocket and is in a position to coordinate Ga/FeEnt-binding; however it is not structurally conserved in ViuP. A

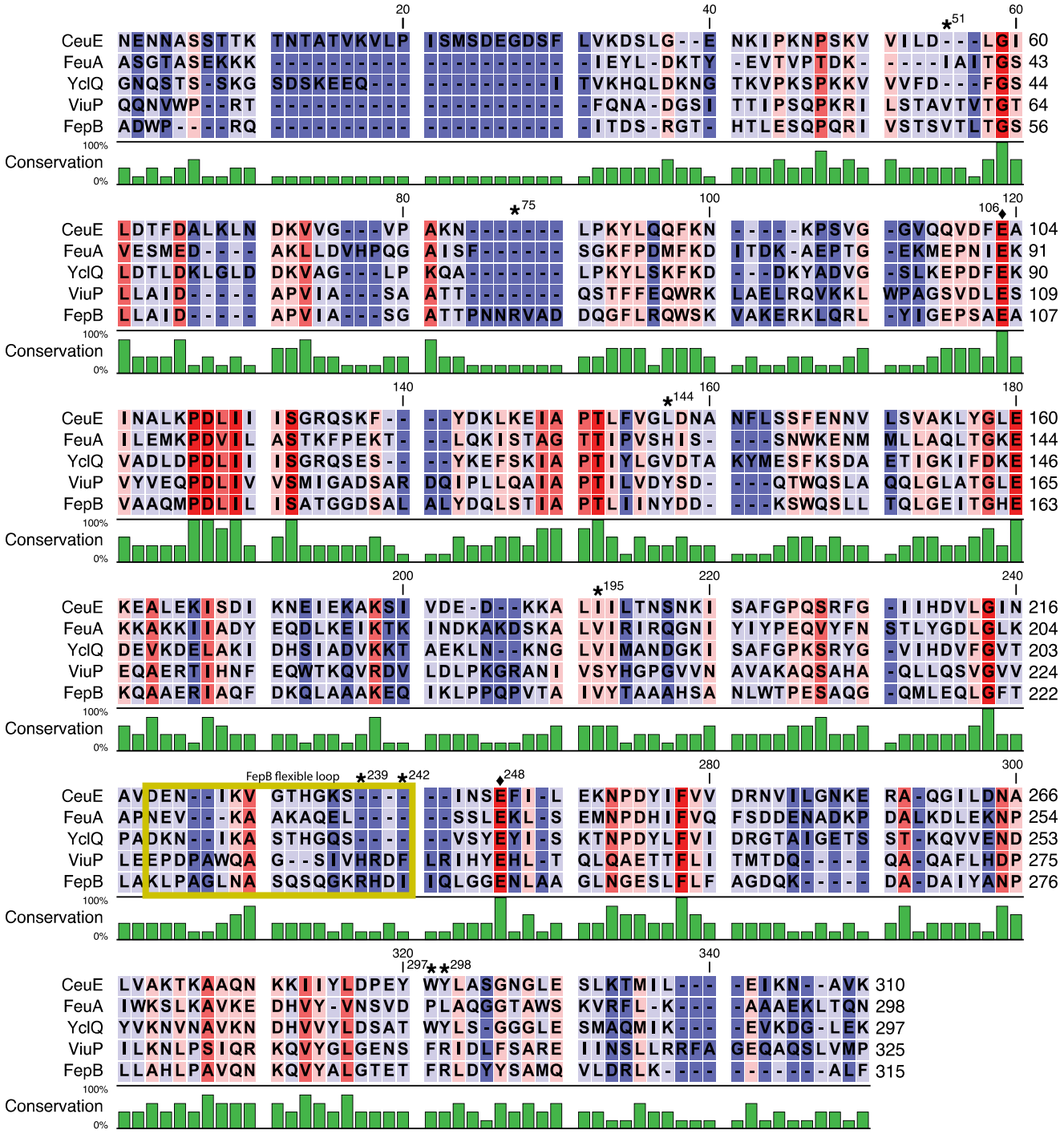

FIGURE 12. **A structure-based sequence alignment of PBPs that bind catecholate-type siderophores.** The sequences are *highlighted* based on conservation using a scale of *blue* to *red*, with the conservation values (%) shown in column format *below* the sequences. *Numbering* based on alignment position and *residue numbers* are shown above and on the right of the sequences, respectively. Important residue positions implicated in Fe/GaEnt binding by FepB are indicated by *numbered asterisks* (*) above the alignment; The flexible loop region of FepB (residues 225–242) is *boxed* in *yellow* and denoted; FepB residues expected to interact with FepD are indicated by *diamonds* (♦). The sequence alignment was constructed using 3D-Coffee (92).

third basic residue to coordinate Ga/FeEnt in holo-FepB could not be readily identified based on sequence conservation alone, but careful examination of the structure revealed that Arg-75 is a prime candidate because of its position in the binding pocket. Interestingly, Arg-75 is part of a structural insert (residues 72–78) that is absent in ViuP (Fig. 12). Although two of three basic coordinating residues differ between FepB and ViuP, there exists significant similarity in their binding pocket composition. This includes the ViuP-FeVib-contacting residues Tyr-146, His-239–Phe-242, and Phe-296. In FepB, CSP and ncSPC secondary structure difference data indicate that the homologous regions Tyr-144–Asp-146, Pro-227–Ile-242, and Thr-294–Tyr-302 are significantly affected by GaEnt binding. Tyr-144 is notable as it aligns with Tyr-146 of ViuP and other type III PBPs that bind catecholate-type siderophores (*e.g.* CeuE and YclQ) and also use a Tyr residue to help coordinate ligand

binding. Our methyl cross-saturation data also implicate Val-51, Val-195, and Ile-242 in the interaction with GaEnt, and the homologous residues in ViuP (Val-59, Ser-197, and Phe-242, respectively) are involved in FeVib binding. Taken together, our NMR data strongly suggest that FepB possesses a ligand binding pocket similar to that of ViuP, with the primary difference being residues 72–78, which provide a coordinating residue (*i.e.* Arg-75) for Ga/FeEnt binding.

From our NMR relaxation experiments, the flexible loop region 233–242 in apo-FepB becomes more ordered upon ligand binding. This increased rigidity likely originates from direct interactions with GaEnt, as observed with Ile-242 (Fig. 8). This loop would provide a favorable electrostatic and hydrogen-bonding environment for Ga/FeEnt (Gln-234, Gln-236, Lys-238, and Arg-239) and could provide a basic ligand-coordinating residue (*i.e.* Arg-239). The movement and direct involvement of C-lobe loop residues in ligand binding has been observed previously for the type III substrate-binding proteins HtsA (90) and SirA (91) from *Staphylococcus aureus*. Interestingly, the location and loop movement of FepB upon ligand binding is similar to residues 228–258 of HtsA, which moves ~12 Å upon substrate binding. B-factor analysis of ViuP suggests that it may also possess a flexible C-lobe loop region (residues 234–239), which becomes more rigid upon ligand binding but does not change position. In addition to FepB C-lobe loop residues, dynamic changes in regions 77–81 and 293–303 also appear to be important for ligand binding and to facilitate proper coordination of Ga/FeEnt in the binding pocket.

While this manuscript was in preparation, the coordinates for the FepB crystal structure complexed with FeEnt were released from the Protein Data Bank (3TLK). This structure confirms our ligand binding findings and shows that Arg-75, Arg-239, and Arg-298 are the basic trio of residues involved in FeEnt coordination and that the methyl groups of Val-51, Val-195, and Ile-242 contribute to ligand binding. The apo FepB crystal structure remains elusive, which is required for understanding the binding mode and mechanism of FeEnt recognition.

The dynamic mechanism through which FepB is able to bind Ga/FeEnt may also play a role in mediating PBP-transporter interactions. Type III PBPs deliver their ligands to inner membrane ABC transporters in Gram-negative bacteria. This interaction is characterized by salt-bridge contacts formed between conserved acidic residues at the apices of each PBP lobe and basic residues on the periplasmic exposed surface of the transporter (8). Sequence comparison of FepB with ViuP, FeuA, YclQ, and CeuE reveals the conservation of Glu residues 106 and 248, which are expected to contact the individual FepD homodimer chains of the FepCD complex (Fig. 10). Structural alignment of apo- and holo-FepB indicates that Glu-106 is in a similar position in both proteins, but Glu-248 moves ~4 Å upon GaEnt binding. The movement of Glu-248 appears to be related to the ordering of residues within the large loop region (residues 225–242) of FepB, which occurs upon ligand binding and may help to position Glu-248 for contact with FepD. Examination of apo-(PDB code 1N4D) and holo-BtuF (PDB code 1N4A) indicates that residues Glu-72 and Glu-202 are positioned similarly in both forms; however, Glu-202 from BtuF in complex with BtuCD (PDB code 2QI9) moves ~7 Å, resulting in the displacement of the C-lobe and release of ligand. Interestingly, homology modeling of FepD reveals the presence of acidic loops that would be in position to interact with the predominantly basic ordered loop and binding pocket of FepB to potentially disrupt FeEnt binding in a similar manner as thought to be the case for cyanocobalamin release and BtuF-BtuCD (Fig. 10) (79). This result also points to an important role for protein dynamics in PBP-transporter interactions and suggests a mechanism through which FepD can trigger release of FeEnt from FepB, despite its strong ligand binding affinity.

In this study, the mapping of siderophore binding to FepB by a modified reverse methyl-cross saturation NMR experiment was particularly effective in highlighting residues that make hydrophobic contacts with the ligand; this is an effective technique that can be applied to other studies of PBP-ligand interactions. C-lobe loop dynamics were shown to have a significant role in ligand binding in FepB, which highlights the usefulness of our solution NMR approach to studying PBPs. For regions 227–242, 294–302, and 77–81 (within the larger region of residues 70–94) of FepB, the movement of these loops is expected to provide critical contacts with the ligand. Furthermore, our results provide further evidence to suggest that type III PBPs do not undergo large scale Venus flytrap opening-closing motions and instead show that subtle bending of the interdomain α-helix leads to modest displacement of the N-lobe toward the C-lobe.

The additional flexibility of PBPs as suggested by this study of FepB is likely also important for ligand dissociation. The role of protein dynamics in ligand release from the PBP to its cognate cytoplasmic membrane ABC transporter is currently not well understood. As suggested by the more open BtuF structure in complex with its cytoplasmic membrane ABC transporter, BtuCD, protein dynamics may play an important role in enabling the C-lobe of BtuF to pivot and spread apart leading to release of cyanocobalamin (79). In the case of FepB-FepCD interactions, the displacement of FeEnt by the proposed highly acidic interacting loops of FepD may involve the highly flexible loop region of FepB. Further elucidation of the dynamic properties of other type III PBPs will improve our understanding of how these proteins are able to tightly (K_d ~nM) bind and release their ligands.

Acknowledgments—We are grateful to the late Dr. Deane McIntyre for maintaining the NMR spectrometers in Calgary. We thank Dr. Peter Tieleman for the use of the cluster computing resources in calculating the FepB structures. We also thank Dr. Hiroaki Ishida for helpful discussions and testing of the methyl cross-saturation experiments and Dr. Ted Johanson for construction of the E. coli ΔentA BL21 strain.

REFERENCES

1. Chu, B. C., Garcia-Herrero, A., Johanson, T. H., Krewulak, K. D., Lau, C. K., Peacock, R. S., Slavinskaya, Z., and Vogel, H. J. (2010) Siderophore uptake in bacteria and the battle for iron with the host: a bird's eye view. *Biometals* **23,** 601–611
2. Loomis, L. D., and Raymond, K. M. (1991) Solution equilibria of enterobactin and metal-enterobactin complexes. *Inorg. Chem.* **30,** 906–911
3. Abergel, R. J., Clifton, M. C., Pizarro, J. C., Warner, J. A., Shuh, D. K., Strong, R. K., and Raymond, K. N. (2008) The siderocalin/enterobactin

interaction: a link between mammalian immunity and bacterial iron transport. *J. Am. Chem. Soc.* **130,** 11524–11534
4. Fischbach, M. A., Lin, H., Liu, D. R., and Walsh, C. T. (2006) How pathogenic bacteria evade mammalian sabotage in the battle for iron. *Nat. Chem. Biol.* **2,** 132–138
5. Henderson, J. P., Crowley, J. R., Pinkner, J. S., Walker, J. N., Tsukayama, P., Stamm, W. E., Hooton, T. M., and Hultgren, S. J. (2009) Quantitative metabolomics reveals an epigenetic blueprint for iron acquisition in uropathogenic *Escherichia coli*. *PLoS Pathog.* **5,** e1000305
6. Watts, R. E., Totsika, M., Challinor, V. L., Mabbett, A. N., Ulett, G. C., De Voss, J. J., and Schembri, M. A. (2012) Contribution of siderophore systems to growth and urinary tract colonization of asymptomatic bacteriuria *Escherichia coli*. *Infect. Immun.* **80,** 333–344
7. Gehring, A. M., Mori, I., and Walsh, C. T. (1998) Reconstitution and characterization of the *Escherichia coli* enterobactin synthetase from EntB, EntE, and EntF. *Biochemistry* **37,** 2648–2659
8. Krewulak, K. D., and Vogel, H. J. (2008) Structural biology of bacterial iron uptake. *Biochim. Biophys. Acta* **1778,** 1781–1804
9. Buchanan, S. K., Smith, B. S., Venkatramani, L., Xia, D., Esser, L., Palnitkar, M., Chakraborty, R., van der Helm, D., and Deisenhofer, J. (1999) Crystal structure of the outer membrane active transporter FepA from *Escherichia coli*. *Nat. Struct. Biol.* **6,** 56–63
10. Annamalai, R., Jin, B., Cao, Z., Newton, S. M., and Klebba, P. E. (2004) Recognition of ferric catecholates by FepA. *J. Bacteriol.* **186,** 3578–3589
11. Barnard, T. J., Watson, M. E., Jr., and McIntosh, M. A. (2001) Mutations in the *Escherichia coli* receptor FepA reveal residues involved in ligand binding and transport. *Mol. Microbiol.* **41,** 527–536
12. Chu, B. C., and Vogel, H. J. (2011) A structural and functional analysis of type III periplasmic and substrate binding proteins: their role in bacterial siderophore and heme transport. *Biol. Chem.* **392,** 39–52
13. Felder, C. B., Graul, R. C., Lee, A. Y., Merkle, H. P., and Sadee, W. (1999) The Venus flytrap of periplasmic binding proteins: an ancient protein module present in multiple drug receptors. *AAPS PharmSci.* **1,** E2
14. Mao, B., Pear, M. R., McCammon, J. A., and Quiocho, F. A. (1982) Hinge-bending in L-arabinose-binding protein: the "Venus's-flytrap" model. *J. Biol. Chem.* **257,** 1131–1133
15. Sharff, A. J., Rodseth, L. E., and Quiocho, F. A. (1993) Refined 1.8-A structure reveals the mode of binding of β-cyclodextrin to the maltodextrin binding protein. *Biochemistry* **32,** 10553–10559
16. Stockner, T., Vogel, H. J., and Tieleman, D. P. (2005) A salt-bridge motif involved in ligand binding and large-scale domain motions of the maltose-binding protein. *Biophys. J.* **89,** 3362–3371
17. Sun, Y. J., Rose, J., Wang, B. C., and Hsiao, C. D. (1998) The structure of glutamine-binding protein complexed with glutamine at 1.94 A resolution: comparisons with other amino acid binding proteins. *J. Mol. Biol.* **278,** 219–229
18. Krewulak, K. D., Shepherd, C. M., and Vogel, H. J. (2005) Molecular dynamics simulations of the periplasmic ferric-hydroxamate binding protein FhuD. *Biometals* **18,** 375–386
19. Ho, W. W., Li, H., Eakanunkul, S., Tong, Y., Wilks, A., Guo, M., and Poulos, T. L. (2007) Holo- and apo-bound structures of bacterial periplasmic heme-binding proteins. *J. Biol. Chem.* **282,** 35796–35802
20. Karpowich, N. K., Huang, H. H., Smith, P. C., and Hunt, J. F. (2003) Crystal structures of the BtuF periplasmic-binding protein for vitamin B12 suggest a functionally important reduction in protein mobility upon ligand binding. *J. Biol. Chem.* **278,** 8429–8434
21. Peuckert, F., Miethke, M., Albrecht, A. G., Essen, L. O., and Marahiel, M. A. (2009) Structural basis and stereochemistry of triscatecholate siderophore binding by FeuA. *Angew. Chem. Int. Ed. Engl.* **48,** 7924–7927
22. Mattle, D., Zeltina, A., Woo, J. S., Goetz, B. A., and Locher, K. P. (2010) Two stacked heme molecules in the binding pocket of the periplasmic heme-binding protein HmuT from *Yersinia pestis*. *J. Mol. Biol.* **404,** 220–231
23. Kandt, C., Xu, Z., and Tieleman, D. P. (2006) Opening and closing motions in the periplasmic vitamin B12-binding protein BtuF. *Biochemistry* **45,** 13284–13292
24. Liu, M., Su, J. G., Kong, R., Sun, T. G., Tan, J. J., Chen, W. Z., and Wang, C. X. (2008) Molecular dynamics simulations of the bacterial periplasmic heme-binding proteins ShuT and PhuT. *Biophys. Chem.* **138,** 42–49
25. Hwang, P. M., Skrynnikov, N. R., and Kay, L. E. (2001) Domain orientation in β-cyclodextrin-loaded maltose-binding protein: diffusion anisotropy measurements confirm the results of a dipolar coupling study. *J. Biomol. NMR* **20,** 83–88
26. Skrynnikov, N. R., Goto, N. K., Yang, D., Choy, W. Y., Tolman, J. R., Mueller, G. A., and Kay, L. E. (2000) Orienting domains in proteins using dipolar couplings measured by liquid-state NMR: differences in solution and crystal forms of maltodextrin binding protein loaded with β-cyclodextrin. *J. Mol. Biol.* **295,** 1265–1273
27. Sharff, A. J., Rodseth, L. E., Spurlino, J. C., and Quiocho, F. A. (1992) Crystallographic evidence of a large ligand-induced hinge-twist motion between the two domains of the maltodextrin-binding protein involved in active transport and chemotaxis. *Biochemistry* **31,** 10657–10663
28. Grzesiek, S., Anglister, J., Ren, H., and Bax, A. (1993) ^{13}C line narrowing by ^{2}H decoupling in $^{2}H/^{13}C/^{15}N$-enriched proteins: application to triple resonance 4D *J* connectivity of sequential amides. *J. Am. Chem. Soc.* **115,** 4369–4370
29. Pervushin, K., Riek, R., Wider, G., and Wüthrich, K. (1997) Attenuated T2 relaxation by mutual cancellation of dipole-dipole coupling and chemical shift anisotropy indicates an avenue to NMR structures of very large biological macromolecules in solution. *Proc. Natl. Acad. Sci. U.S.A.* **94,** 12366–12371
30. Otten, R., Chu, B., Krewulak, K. D., Vogel, H. J., and Mulder, F. A. (2010) Comprehensive and cost-effective NMR spectroscopy of methyl groups in large proteins. *J. Am. Chem. Soc.* **132,** 2952–2960
31. Gardner, K. H., and Kay, L. E. (1997) Production and incorporation of $^{15}N,^{13}C,^{2}H$ (^{1}H-δ1 methyl) isoleucine into proteins for multidimensional NMR studies. *J. Am. Chem. Soc.* **119,** 7599–7600
32. Goto, N. K., Gardner, K. H., Mueller, G. A., Willis, R. C., and Kay, L. E. (1999) A robust and cost-effective method for the production of Val, Leu, Ile (δ1) methyl-protonated ^{15}N-,^{13}C-,^{2}H-labeled proteins. *J. Biomol NMR* **13,** 369–374
33. Elkins, M. F., and Earhart, C. F. (1989) Nucleotide sequence and regulation of the *Escherichia coli* gene for ferrienterobactin transport protein FepB. *J. Bacteriol.* **171,** 5443–5451
34. Tugarinov, V., Kanelis, V., and Kay, L. E. (2006) Isotope labeling strategies for the study of high-molecular-weight proteins by solution NMR spectroscopy. *Nat. Protoc.* **1,** 749–754
35. Liu, J., Duncan, K., and Walsh, C. T. (1989) Nucleotide sequence of a cluster of *Escherichia coli* enterobactin biosynthesis genes: identification of *entA* and purification of its product, 2,3-dihydro-2,3-dihydroxybenzoate dehydrogenase. *J. Bacteriol.* **171,** 791–798
36. André, I., and Linse, S. (2002) Measurement of Ca^{2+}-binding constants of proteins and presentation of the CaLigator software. *Anal. Biochem.* **305,** 195–205
37. Rohrbach, M. R., Braun, V., and Köster, W. (1995) Ferrichrome transport in *Escherichia coli* K-12: altered substrate specificity of mutated periplasmic FhuD and interaction of FhuD with the integral membrane protein FhuB. *J. Bacteriol.* **177,** 7186–7193
38. Eletsky, A., Kienhofer, A., and Pervushin, K. (2001) TROSY NMR with partially deuterated proteins. *J. Biomol NMR* **20,** 177–180
39. Salzmann, M., Pervushin, K., Wider, G., Senn, H., and Wuthrich, K. (1998) TROSY in triple-resonance experiments: new perspectives for sequential NMR assignment of large proteins. *Proc. Natl. Acad. Sci. U.S.A.* **95,** 13585–13590
40. Salzmann, M., Wider, G., Pervushin, K., Senn, H., and Wuthrich, K. (1999) TROSY-type triple resonance experiments for sequential NMR assignments of large proteins. *J. Am. Chem. Soc.* **121,** 844–848
41. Zhu, G., Xia, Y., Nicholson, L. K., and Sze, K. H. (2000) Protein dynamics measurements by TROSY-based NMR experiments. *J. Magn. Reson.* **143,** 423–426
42. Hansen, M. R., Mueller, L., and Pardi, A. (1998) Tunable alignment of macromolecules by filamentous phage yields dipolar coupling interactions. *Nat. Struct. Biol.* **5,** 1065–1074
43. Ottiger, M., Delaglio, F., and Bax, A. (1998) Measurement of *J* and dipolar couplings from simplified two-dimensional NMR spectra. *J. Magn. Reson.* **131,** 373–378

44. Zhu, G., Kong, X. M., and Sze, K. H. (1999) Gradient and sensitivity enhancement of 2D TROSY with water flip-back, 3D NOESY-TROSY, and TOCSY-TROSY experiments. *J. Biomol. NMR* **13,** 77–81
45. Orekhov, V. Y., Ibraghimov, I., and Billeter, M. (2003) Optimizaing resolution in multidimensional NMR by three-way decomposition. *J. Biomol. NMR* **27,** 165–173
46. Takahashi, H., Miyazawa, M., Ina, Y., Fukunishi, Y., Mizukoshi, Y., Nakamura, H., and Shimada, I. (2006) Utilization of methyl proton resonances in cross-saturation measurement for determining the interfaces of large protein-protein complexes. *J. Biomol. NMR* **34,** 167–177
47. Huang, H., and Vogel, H. J. (2012) Structural basis for the activation of platelet integrin αIIbβ3 by calcium- and integrin-binding protein 1. *J. Am. Chem. Soc.* **134,** 3864–3872
48. Geen, H., and Freeman, R. (1991) Band-selective radiofrequency pulses. *J. Magn. Reson.* **93,** 93–141
49. Mulder, F. A., Schipper, D., Bott, R., and Boelens, R. (1999) Altered flexibility in the substrate-binding site of related native and engineered high-alkaline *Bacillus subtilisins*. *J. Mol. Biol.* **292,** 111–123
50. Goddard, T. D., and Kneller, D. G. (2003) *Sparky 3*, University of California, San Francisco
51. Barbato, G., Ikura, M., Kay, L. E., Pastor, R. W., and Bax, A. (1992) Backbone dynamics of calmodulin studied by ^{15}N relaxation using inverse detected two-dimensional NMR spectroscopy: the central helix is flexible. *Biochemistry* **31,** 5269–5278
52. Eswar, N., John, B., Mirkovic, N., Fiser, A., Ilyin, V. A., Pieper, U., Stuart, A. C., Marti-Renom, M. A., Madhusudhan, M. S., Yerkovich, B., and Sali, A. (2003) Tools for comparative protein structure modeling and analysis. *Nucleic Acids Res.* **31,** 3375–3380
53. Sali, A., and Blundell, T. L. (1993) Comparative protein modelling by satisfaction of spatial restraints. *J. Mol. Biol.* **234,** 779–815
54. Li, N., Zhang, C., Li, B., Liu, X., Huang, Y., Xu, S., and Gu, L. (2012) Unique iron coordination in iron-chelating molecule vibriobactin helps *Vibrio cholerae* evade mammalian siderocalin-mediated immune response. *J. Biol. Chem.* **287,** 8912–8919
55. Gardner, K. H., Rosen, M. K., and Kay, L. E. (1997) Global folds of highly deuterated methyl-protonated proteins by multidimensonal NMR. *Biochemistry* **36,** 1389–1401
56. Venters, R. A., Farmer, B. T., 2nd, Fierke, C. A., and Spicer, L. D. (1996) Characterizing the use of perdeuteration in NMR studies of large proteins. *J. Mol. Biol.* **264,** 1101–1116
57. Wishart, D. S., and Sykes, B. D. (1994) The ^{13}C chemical-shift index: a simple method for the identification of protein secondary structure using 13C chemical-shift data. *J. Biomol. NMR* **4,** 171–180
58. Shen, Y., Delaglio, F., Cornilescu, G., and Bax, A. (2009) TALOS+: a hybrid method for predicting protein backbone torsion angles from NMR chemical shifts. *J. Biomol. NMR* **44,** 213–223
59. Tugarinov, V., Choy, W. Y., Orekhov, V. Y., and Kay, L. E. (2005) Solution NMR-derived global fold of a monomeric 82-kDa enzyme. *Proc. Natl. Acad. Sci. U.S.A.* **102,** 622–627
60. Tjandra, N., Omichinski, J. G., Gronenborn, A. M., Clore, G. M., and Bax, A. (1997) Use of dipolar ^{1}H-^{15}N and ^{1}H-^{13}C couplings in the structure determination of magnetically oriented macromolecules in solution. *Nat. Struct. Biol.* **4,** 732–738
61. Tolman, J. R., Flanagan, J. M., Kennedy, M. A., and Prestegard, J. H. (1995) Nuclear magnetic dipole interactions in field-oriented proteins: information for structure determination in solution. *Proc. Natl. Acad. Sci. U.S.A.* **92,** 9279–9283
62. Schwieters, C. D., Kuszewski, J. J., Tjandra, N., and Clore, G. M. (2003) The Xplor-NIH NMR molecular structure determination package. *J. Magn. Reson.* **160,** 65–73
63. Chou, J. J., Li, S., and Bax, A. (2000) Study of conformational rearrangement and refinement of structural homology models by the use of heteronuclear dipolar couplings. *J. Biomol. NMR* **18,** 217–227
64. Chu, B. C., DeWolf, T., and Vogel, H. J. (2013) The role of the two structural domains from the periplasmic *E. coli* histidine binding protein HisJ. *J. Biol. Chem.* **288,** 31409–31422
65. Gifford, J. L., Ishida, H., and Vogel, H. J. (2011) Fast methionine-based solution structure determination of calcium-calmodulin complexes. *J. Biomol. NMR* **50,** 71–81
66. Bhattacharya, A., Tejero, R., and Montelione, G. T. (2007) Evaluating protein structures determined by structural genomics consortia. *Proteins* **66,** 778–795
67. Llinás, M., Wilson, D. M., and Neilands, J. B. (1973) Effect of metal binding on the conformation of enterobactin: proton and carbon-13 nuclear magnetic resonance study. *Biochemistry* **12,** 3836–3843
68. Usher, K. C., Ozkan, E., Gardner, K. H., and Deisenhofer, J. (2001) The plug domain of FepA, a TonB-dependent transport protein from *Escherichia coli*, binds its siderophore in the absence of the transmembrane barrel domain. *Proc. Natl. Acad. Sci. U.S.A.* **98,** 10676–10681
69. Peacock, R. S., Andrushchenko, V. V., Demcoe, A. R., Gehmlich, M., Lu, L. S., Herrero, A. G., and Vogel, H. J. (2006) Characterization of TonB interactions with the FepA cork domain and FecA N-terminal signaling domain. *Biometals* **19,** 127–142
70. Tamiola, K., Acar, B., and Mulder, F. A. (2010) Sequence-specific random coil chemical shifts of intrinsically disordered proteins. *J. Am. Chem. Soc.* **132,** 18000–18003
71. Tamiola, K., and Mulder, F. A. (2012) Using NMR chemical shifts to calculate the propensity for structural order and disorder in proteins. *Biochem. Soc. Trans.* **40,** 1014–1020
72. Sprencel, C., Cao, Z., Qi, Z., Scott, D. C., Montague, M. A., Ivanoff, N., Xu, J., Raymond, K. M., Newton, S. M., and Klebba, P. E. (2000) Binding of ferric enterobactin by the *Escherichia coli* periplasmic protein FepB. *J. Bacteriol.* **182,** 5359–5364
73. Takahashi, H., Nakanishi, T., Kami, K., Arata, Y., and Shimada, I. (2000) A novel NMR method for determining the interfaces of large protein-protein complexes. *Nat. Struct. Biol.* **7,** 220–223
74. Shimada, I., Ueda, T., Matsumoto, M., Sakakura, M., Osawa, M., Takeuchi, K., Nishida, N., and Takahashi, H. (2009) Cross-saturation and transferred cross-saturation experiments. *Prog. Nucl. Mag. Res. Sp.* **54,** 123–140
75. Takeda, M., Terasawa, H., Sakakura, M., Yamaguchi, Y., Kajiwara, M., Kawashima, H., Miyasaka, M., and Shimada, I. (2003) Hyaluronan recognition mode of CD44 revealed by cross-saturation and chemical shift perturbation experiments. *J. Biol. Chem.* **278,** 43550–43555
76. Coudevylle, N., Geist, L., Hötzinger, M., Hartl, M., Kontaxis, G., Bister, K., and Konrat, R. (2010) The v-myc-induced Q83 lipocalin is a siderocalin. *J. Biol. Chem.* **285,** 41646–41652
77. Abergel, R. J., Warner, J. A., Shuh, D. K., and Raymond, K. N. (2006) Enterobactin protonation and iron release: structural characterization of the salicylate coordination shift in ferric enterobactin. *J. Am. Chem. Soc.* **128,** 8920–8931
78. Ortega, A., Amorós, D., and García de la Torre, J. (2011) Prediction of hydrodynamic and other solution properties of rigid proteins from atomic- and residue-level models. *Biophys. J.* **101,** 892–898
79. Hvorup, R. N., Goetz, B. A., Niederer, M., Hollenstein, K., Perozo, E., and Locher, K. P. (2007) Asymmetry in the structure of the ABC transporter-binding protein complex BtuCD-BtuF. *Science* **317,** 1387–1390
80. Bermejo, G. A., Strub, M. P., Ho, C., and Tjandra, N. (2010) Ligand-free open-closed transitions of periplasmic binding proteins: the case of glutamine-binding protein. *Biochemistry* **49,** 1893–1902
81. Hayward, S., and Berendsen, H. J. (1998) Systematic analysis of domain motions in proteins from conformational change: new results on citrate synthase and T4 lysozyme. *Proteins* **30,** 144–154
82. Trakhanov, S., Vyas, N. K., Luecke, H., Kristensen, D. M., Ma, J., and Quiocho, F. A. (2005) Ligand-free and -bound structures of the binding protein (LivJ) of the *Escherichia coli* ABC leucine/isoleucine/valine transport system: trajectory and dynamics of the interdomain rotation and ligand specificity. *Biochemistry* **44,** 6597–6608
83. Sobolev, V., Eyal, E., Gerzon, S., Potapov, V., Babor, M., Prilusky, J., and Edelman, M. (2005) SPACE: a suite of tools for protein structure prediction and analysis based on complementarity and environment. *Nucleic Acids Res.* **33,** W39–W43
84. Berntsson, R. P., Smits, S. H., Schmitt, L., Slotboom, D. J., and Poolman, B. (2010) A structural classification of substrate-binding proteins. *FEBS Lett.* **584,** 2606–2617
85. Holm, L., and Rosenström, P. (2010) Dali server: conservation mapping in 3D. *Nucleic Acids Res.* **38,** W545–W549

86. Krissinel, E., and Henrick, K. (2004) Secondary-structure matching (SSM), a new tool for fast protein structure alignment in three dimensions. *Acta Crystallogr. D Biol. Crystallogr.* **60,** 2256–2268
87. Raymond, K. N., Dertz, E. A., and Kim, S. S. (2003) Enterobactin: an archetype for microbial iron transport. *Proc. Natl. Acad. Sci. U.S.A.* **100,** 3584–3588
88. Müller, A., Wilkinson, A. J., Wilson, K. S., and Duhme-Klair, A. K. (2006) An $[\{Fe(mecam)\}_2]^{6-}$ bridge in the crystal structure of a ferric enterobactin-binding protein. *Angew. Chem. Int. Ed. Engl.* **45,** 5132–5136
89. Zawadzka, A. M., Kim, Y., Maltseva, N., Nichiporuk, R., Fan, Y., Joachimiak, A., and Raymond, K. N. (2009) Characterization of a *Bacillus subtilis* transporter for petrobactin, an anthrax stealth siderophore. *Proc. Natl. Acad. Sci. U.S.A.* **106,** 21854–21859
90. Grigg, J. C., Cooper, J. D., Cheung, J., Heinrichs, D. E., and Murphy, M. E. (2010) The *Staphylococcus aureus* siderophore receptor HtsA undergoes localized conformational changes to enclose staphyloferrin A in an arginine-rich binding pocket. *J. Biol. Chem.* **285,** 11162–11171
91. Grigg, J. C., Cheung, J., Heinrichs, D. E., and Murphy, M. E. (2010) Specificity of staphyloferrin B recognition by the SirA receptor from *Staphylococcus aureus*. *J. Biol. Chem.* **285,** 34579–34588
92. Di Tommaso, P., Moretti, S., Xenarios, I., Orobitg, M., Montanyola, A., Chang, J. M., Taly, J. F., and Notredame, C. (2011) T-Coffee: a Web server for the multiple sequence alignment of protein and RNA sequences using structural information and homology extension. *Nucleic Acids Res.* **39,** W13–W17
93. Dundas, J., Ouyang, Z., Tseng, J., Binkowski, A., Turpaz, Y., and Liang, J. (2006) CASTp: computed atlas of surface topography of proteins with structural and topographical mapping of functionally annotated residues. *Nucleic Acids Res.* **34,** W116–W118
94. Krewulak, K. D., Koster, W., and Vogel, H. J. (2009) Siderophore-binding protein FhuD and related periplasmic proteins involved in bacterial iron uptake, in *Handbook of Metalloproteins* (Messerschmidt, A., ed), John Wiley & Sons, Inc., New York

The Solution Structure, Binding Properties, and Dynamics of the Bacterial Siderophore-binding Protein FepB

Byron C. H. Chu, Renee Otten, Karla D. Krewulak, Frans A. A. Mulder and Hans J. Vogel

J. Biol. Chem. 2014, 289:29219-29234.
doi: 10.1074/jbc.M114.564021 originally published online August 29, 2014